AGU PUBLICATIONS

JGR

Journal of Geophysical Research: Solid Earth

RESEARCH ARTICLE
10.1002/2015JB012676

Key Points:
- Microstructure of shale is explicitly represented
- Particle-scale mechanisms are elucidated
- Effect of various factors is evaluated

Correspondence to:
C. Y. Kwok,
fkwok8@hku.hk

Citation:
Duan, K., and C. Y. Kwok (2016), Evolution of stress-induced borehole breakout in inherently anisotropic rock: Insights from discrete element modeling, *J. Geophys. Res. Solid Earth*, *121*, 2361–2381, doi:10.1002/2015JB012676.

Received 20 NOV 2015
Accepted 1 APR 2016
Accepted article online 6 APR 2016
Published online 18 APR 2016

Evolution of stress-induced borehole breakout in inherently anisotropic rock: Insights from discrete element modeling

K. Duan[1] and C. Y. Kwok[1]

[1]Department of Civil Engineering, University of Hong Kong, Hong Kong

Abstract The aim of this study is to better understand the mechanisms controlling the initiation, propagation, and ultimate pattern of borehole breakouts in shale formation when drilled parallel with and perpendicular to beddings. A two-dimensional discrete element model is constructed to explicitly represent the microstructure of inherently anisotropic rocks by inserting a series of individual smooth joints into an assembly of bonded rigid discs. Both isotropic and anisotropic hollow square-shaped samples are generated to represent the wellbores drilled perpendicular to and parallel with beddings at reduced scale. The isotropic model is validated by comparing the stress distribution around borehole wall and along *X* axis direction with analytical solutions. Effects of different factors including the particle size distribution, borehole diameter, far-field stress anisotropy, and rock anisotropy are systematically evaluated on the stress distribution and borehole breakout propagation. Simulation results reveal that wider particle size distribution results in the local stress perturbations which cause localization of cracks. Reduction of borehole diameter significantly alters the crack failure from tensile to shear and raises the critical pressure. Rock anisotropy plays an important role on the stress state around wellbore which lead to the formation of preferred cracks under hydrostatic stress. Far-field stress anisotropy plays a dominant role in the shape of borehole breakout when drilled perpendicular to beddings while a secondary role when drilled parallel with beddings. Results from this study can provide fundamental insights on the underlying particle-scale mechanisms for previous findings in laboratory and field on borehole stability in anisotropic rock.

1. Introduction

Shales make up more than 75% of drilled oil and gas formations worldwide and cause most wellbore-instability problems during and after drilling. The drilling cost attributed to shale-instability problems is reported to be in excess of one half billion U.S. dollars per year. Shales are inherently anisotropic in both stiffness and strength due to their laminated structure which induce a complicated stress field in the circumference of the borehole [*Amadei*, 1996]. The drilling process imposes stress redistribution which will lead to the creation of a so-called excavation damage zone. Rock failure around the boreholes often results in certain types of failure zones, which are valuable indicators of the minimum principle stress direction [*Zoback et al*., 2003, 1985]. Failure mechanisms of boreholes in planes of weakness are still not fully understood. Wellbore instability is a multiple parameter-dependent phenomenon as the formation of borehole breakouts is dominated by several factors, e.g., the in situ stress, the material properties, the borehole diameter, and the support system [*Brudy and Zoback*, 1999; *Zhang*, 2013]. Understanding borehole failure mechanism is important in optimizing well production, in efforts to design stable wellbores, as well as in attempting to utilize the breakout shape for in situ stress determination [*Haimson and Song*, 1993].

The formation of breakouts around borehole walls and underground opening has been studied extensively in field, laboratory, and numerical modeling. Borehole problems in field appear to be caused by instability related to bedding plane splitting rather to the conventional shear failure often encountered in boreholes [*Kupferschmied et al*., 2015; *Labiouse and Vietor*, 2014]. In laboratory, reduced-scale experiments have been extensively conducted to elucidate the mechanisms and process of stress-induced borehole breakouts [*Dresen et al*., 2010; *Ewy and Cook*, 1990a, 1990b; *Haimson and Song*, 1993; *Lee and Haimson*, 1993; *Zheng et al*., 1989]. The detailed cross-sectional shape of stress-induced wellbore breakouts has been studied. Various modes have been reported in literatures, including the spiral-shaped [*Meier et al*., 2013], V-shaped (or dog-eared), slot-like breakouts [*Haimson*, 2007; *Haimson and Kovacich*, 2003; *Haimson and Lee*, 2004] and bedding-dominated breakouts [*Meier et al*., 2014]. The hollow cylinder simulation experiments have revealed a very strong influence of the angle between the borehole axis and the bedding plane of the shale [*Labiouse and Vietor*, 2014; *Meier et al*., 2013; *Ong and Roegiers*, 1993]. The samples cored in direction

perpendicular to and parallel with the bedding planes behave very differently. For the former case, spiral-shaped shear fractures develop symmetrically around the borehole [*Meier et al*., 2014]. For the latter one, shear failure along conjugated planes was found in the plastic Boom Clay [*François et al*., 2014; *Labiouse et al*., 2014], while bedding plane splitting and bulking emerged in the indurated Opalinus Clay [*Blümling et al*., 2007; *Labiouse and Vietor*, 2014] and other shale formations [*Ong and Roegiers*, 1993]. It is not completely clear in what direction the fractures grow to create a spalled piece and in what mode the failure occurs and whether failure occurs first in rock matrix or weak layer [*Labiouse et al*., 2014].

Most rock mechanics analyses on stability of openings in rock formations should involve two key steps, first, the calculation of stress distribution around the borehole and then the application of failure criteria to predict failure [*Al-Ajmi and Zimmerman*, 2006; *Gaede et al*., 2012; *Ong and Roegiers*, 1993; *Zheng et al*., 1989; *Zoback et al*., 1985]. Among the numerous proposed models in the literature, a linear elastic and isotropic constitutive model, in conjunction with a linear failure criterion, is perhaps the most common approach. However, shale is known to exhibit anisotropic properties both for deformation and failure due to their laminated structure. Although analytical solution of the near-wellbore stress distribution in anisotropic formations has been developed [*Amadei et al*., 1983; *Gaede et al*., 2012, 2013] and anisotropic rock strength criterion has been applied to evaluate the damage of the formation in the borehole vicinity [*Lee et al*., 2012; *Zhang*, 2013], stress redistribution after the creation of fractures is a dynamic process and the evolution of failure is difficult to be modeled by constitutive method. To this end, the micromechanics-based approach, such as the Discrete Element Method (DEM), may assist in understanding the physical process and underlying mechanisms of borehole breakouts under different drilling directions, in situ stresses, borehole diameters, and anisotropy angles.

The particle-based DEM method [*Cundall and Strack*, 1979] has been applied in the studying of breakout geometries and their formation mechanisms around openings in rock [*Al-Busaidi et al*., 2005; *Cook et al*., 2004; *Fakhimi et al*., 2002; *Potyondy and Cundall*, 2004]. In particular, the failure process and underlying mechanisms of fracture-like borehole breakouts in porous sandstones have been examined based on the grain breakage [*Lee et al*., 2015] and grain-crushing algorithm [*Rahmati et al*., 2014]. However, all of the previous studies were performed on the isotropic model where the effects of rock anisotropy are ignored. Based on the synthetic rock mass model [*Ivars et al*., 2011], DEM has been applied in the investigation of anisotropic behaviors of jointed rock mass [*Bahaaddini et al*., 2013; *Chiu et al*., 2013]. But one should expect that for smaller openings (e.g., borehole) intact rock anisotropy would be more critical than anisotropy created by joints [*Amadei*, 1996].

In this study, the evolution of stress-induced borehole breakout in simulated Mancos shale at laboratory scale is investigated by using a newly developed DEM approach in which the microstructure of intact anisotropic rocks can be explicitly represented by inserting a series of parallel smooth joints into the bonded particle model. The aim of this study is to explore the fracture processes and underlying micromechanisms contributing to different laboratory observations on the breakout of boreholes drilled in anisotropic rocks. In addition, the effects of several factors, e.g., the particle size distribution, borehole diameter, and far-field stress anisotropy, are systematically evaluated.

2. Numerical Methodologies

2.1. Bonded Particle Model

The Particle Flow Code (PFC2D) [*Itasca*, 2008] developed by the Itasca Consulting Group is adopted in this study for the numerical simulations. In the numerical model, rock is represented by bonding an assembly of particles at their contacts, and the equations of motion are solved using a time stepping, explicit scheme [*Cundall and Strack*, 1979; *Potyondy and Cundall*, 2004]. The bond will break if the stress acting on it exceeds the corresponding strength. Once a bond fails, the stress will be redistributed, but this redistribution may not be adequate to rupture the adjacent contacts [*Cho et al*., 2007; *Diederichs*, 2000]. As a result, the crack-generating process in PFC is a stable process such that applied deviatoric boundary stress must be increased to generate new cracks. The advantage of DEM over other continuum methods is its ability to explicitly model the initiation and propagation of cracks from microscale to macroscale without applying complex constitutive laws [*Cundall*, 2001].

2.2. Smooth Joint Model

The smooth joint model was first proposed by *Cundall et al*. [1996] to represent fractures in jointed rock mass. The smooth joint contact model allows particles at the joint surface experience relative slip on the specified

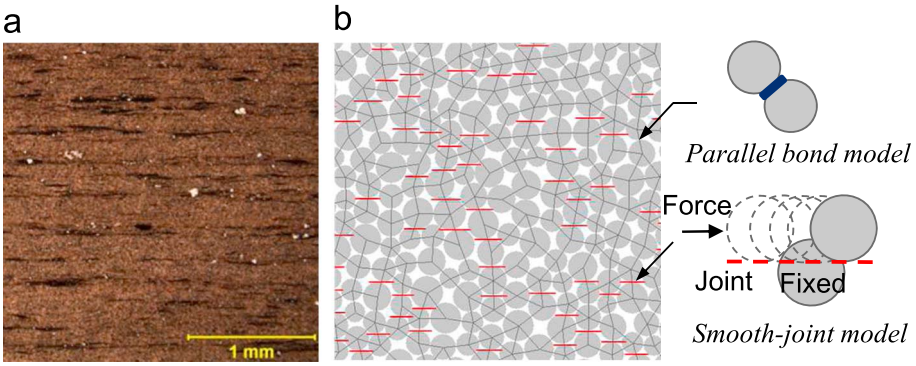

Figure 1. (a) Thin-section image of Bossier Shale [*Ambrose et al*., 2014]. (b) Generation of inherently anisotropic DEM sample based on the bonded particle model (BPM) [*Potyondy and Cundall*, 2004] and the smooth joint model (SJ) [*Mas Ivars et al*., 2008].

joint surface rather than sliding along the particle surface as depicted in Figure 1b. The behavior of joints can be modeled by assigning smooth joint models to all contacts between particles that lie on opposite sides of the joint. At these contacts, parallel bonds are removed and smooth joints are imposed in a direction parallel with the joint planes. In this study, individual smooth joint contacts are imposed on the bonded particle model to explicitly represent the inherent anisotropy of anisotropic rock. The algorithm and procedure for the generation of inherently anisotropic samples will be discussed in the next section.

2.3. Inherently Anisotropic Model

The anisotropic properties of sedimentary rocks, e.g., shale, are caused by the oriented distribution of minerals and organic matters [*Fjær and Nes*, 2014; *Meier et al*., 2013]. Microscopic observations reveal that the discontinuities of intrinsic anisotropy are not necessarily continuous or straight (see Figure 1a) [*Ambrose et al*., 2014]. In order to explicitly represent the microstructure of this type of rock, a novel approach has been proposed by the authors [*Duan and Kwok*, 2015b; *Duan et al*., 2015a] based on the bonded particle model [*Potyondy and Cundall*, 2004] and the smooth joint model [*Ivars et al*., 2011; *Mas Ivars et al*., 2008] as illustrated in Figure 1b. To construct the inherently anisotropic model, a series of rigid discs are first created and bonded at their contacts to represent the rock matrix (bonded particle model). After that any subhorizontal parallel bonds (for instance those dipping within $-10°$ to $+10°$) are removed and replaced with horizontal smooth joint contacts (dipping 0°) to introduce the horizontal anisotropy. Similarly, samples with different anisotropy angles (β, defined as the angle between the normal of beddings and the maximum principal stress direction) can be generated.

Systematic parametric studies have been conducted to evaluate the effect of smooth joint properties (including stiffness, tensile strength, cohesion, friction angle, friction coefficient, and number of weak layers) on the macroscopic response of anisotropic rock model under both uniaxial compression and Brazilian test conditions, based on which a step-by-step calibration procedure is proposed for the efficient selection of microparameters [*Duan and Kwok*, 2015a, 2015b; *Duan et al*., 2015a]. The diverse macroscopic responses between different rock types are found to be controlled by the difference between weak layer properties on particle scale. Various failure modes, i.e., elastic mismatch, sliding wing crack, and compression-induced tensile crack, are found to be the dominant mechanisms when $\beta = 0°$, 45°, and 90°, respectively. It is the transition of these micromechanisms that controls the anisotropic behaviors at sample scale [*Duan and Kwok*, 2015b; *Duan et al*., 2015a; *Kwok and Duan*, 2015]. This numerical approach provides a new way to study the behaviors of inherently anisotropic rocks which can link the strength anisotropy, deformation behaviors, and failure patterns on sample scale to the microstructure and particle-scale properties.

3. Calibration and Validation of Numerical Model

3.1. Calibration

The DEM model is calibrated to represent the mechanical behaviors of Mancos shale [*Fjær and Nes*, 2014] under uniaxial compression test. In the laboratory, unconfined compression tests were conducted on

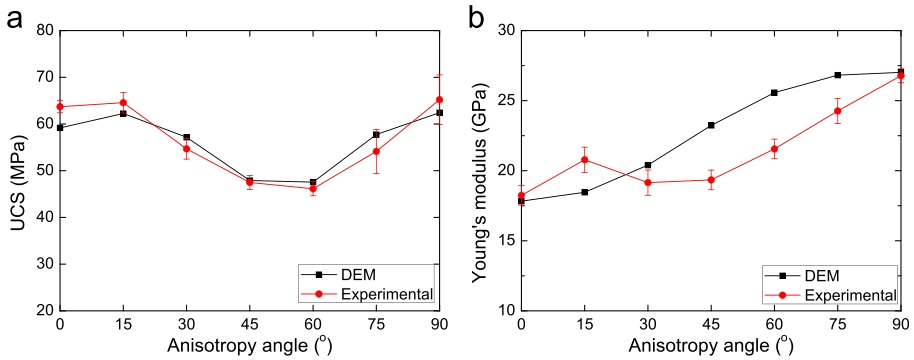

Figure 2. Comparison between the variations of (a) uniaxial compression strength (UCS) and (b) Young's modulus of Mancos Shale from DEM modeling and laboratory tests [*Fjær and Nes*, 2014].

15 mm diameter, 30 mm long specimens drilled at every 15° of inclination. Calibration is conducted on rectangular samples with size 50 mm × 25 mm. The particle size follows a uniform distribution with $R_{min} = 0.075$ mm and $R_{max}/R_{min} = 1.66$. The sample consists of ~37,000 particles, and there are about 125 particles cross the minimum dimension of the specimen. DEM samples with different anisotropy angles ($\beta = 0°$, 15°, 30°, 45°, 60°, 75°, and 90°) are constructed, and uniaxial compression tests are performed on them. Following the recommended procedures [*Duan and Kwok*, 2015a], the microparameters of parallel bond and smooth joint are calibrated to match the variation of uniaxial compression strength (*UCS*) and Young's modulus obtained in laboratory as illustrated in Figures 2a and 2b, respectively. Corresponding microparameters are listed in Table 1. The DEM model can capture the anisotropic characteristics of both strength and deformation properties of Mancos shale, namely, the U-shaped curve of UCS and the constantly increasing-shaped Young's modulus as a function of anisotropy angle, which are also consistent with other anisotropic rocks [*Cho et al*., 2012; *Gatelier et al*., 2002; *Niandou et al*., 1997; *Rawling et al*., 2002].

3.2. Model Generation and Boundary Conditions

The schematic of the numerical model used for the borehole breakout simulation and the adopted loading path are illustrated in Figures 3a and 3b, respectively. Numerical tests are conducted on square samples (50 mm × 50 mm) with a hole in the center ($D = 10$ mm). There are ~71,300 particles in the sample, and about 50 particles cross the borehole diameter. It is worthy emphasizing that the spherical elements are simply a way to discretizing the model. We do not aim to represent the real particle size and size distribution of natural rock due to its heterogeneous and irregular characteristic. The selection of particle size is optimized with regard to the representativeness of the calculation results and the computation time. In previous laboratory studies [*Haimson*, 2007; *Meier et al*., 2014], it was found that samples cored in directions parallel with and perpendicular to the weak layers behave very differently. Thus, these two extreme cases are taken into account in this study. Previous studies have also confirmed that the difference between isotropic and transverse isotropic rock is negligible when the wellbore is drilled perpendicular to beddings [*Meier et al*., 2014]. Hence, the isotropic model without weak layers is adopted to represent the condition when borehole drilled perpendicular to beddings and $\beta_0 = 45°$ is adopted to represent the case when the borehole orientated parallel with weak layers as shown in Figure 3a.

Table 1. Microparameters Calibrated for Mancos Shale

Microparameters		Mancos Shale
Particle	Stiffness, E_c (GPa)	23
	Density, ρ (kg/m^3)	3,169
	Friction coefficient, μ	0.5
Parallel bond	Stiffness, $\bar{E}_c$ (GPa)	23
	Normal strength, $\bar{\sigma}_c$ (MPa)	60 ± 13.5
	Shear strength, $\bar{\tau}_c$ (MPa)	60 ± 13.5
Smooth joint	Angle range	±30°
	Normal stiffness, $\bar{k}_n$ (GPa/m)	43,000
	Shear stiffness, $\bar{k}_s$ (GPa/m)	43,000
	Tensile strength, σ_c (MPa)	30
	Cohesion, c_b (MPa)	22
	Friction coefficient, μ_c	0.5
	Friction angle (°)	0

During the test, the load is applied by moving the top and bottom platens with constant strain rate which is slow enough to ensure quasi-static response ($\dot{\varepsilon} = 0.5\ s^{-1}$). The locations of the two

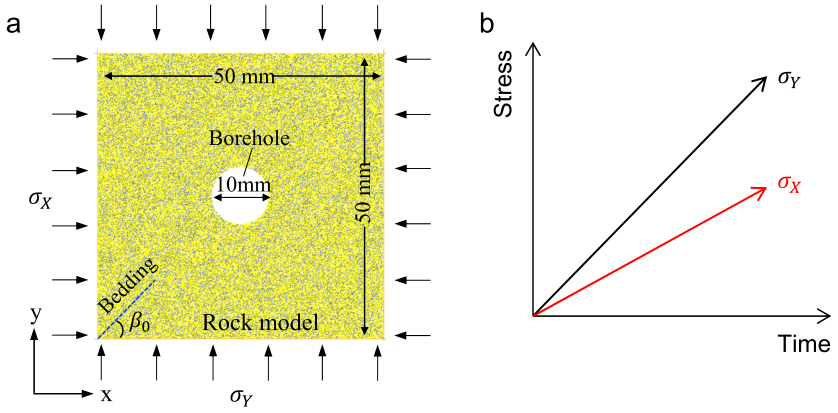

Figure 3. (a) Anisotropic model for stress-induced borehole breakout simulation. (b) Loading condition.

lateral walls are adjusted based on the servomechanism to maintain constant K_0, where $K_0 = \sigma_X/\sigma_Y$. Both σ_X and σ_Y are raised simultaneously until the collapse of borehole. Stresses acting on the platens are recorded, and strains are calculated from the displacement of corresponding platens. In the numerical model, each bond breakage is assumed to be a microcrack which can be classified into four categories: tensile failure of parallel bond (crk_pn_n), shear failure of parallel bond (crk_pb_s), tensile failure of smooth joint (crk_sj_n), and shear failure of smooth joint (crk_sj_s) according to their failure mechanisms. The same nomenclature will be adopted in the following discussions.

3.3. Validation of the Numerical Model

For a cylinder hole in a thick, homogeneous, isotropic elastic plate subjected to effective minimum and maximum far-field principal stresses (σ_h* and σ_H*), the following equations apply [*Haimson*, 2007; *Kirsch*, 1898; *Zoback et al.*, 1985]:

$$\sigma_{rr} = \frac{1}{2}(\sigma_H{}^* + \sigma_h{}^*)\left(1 - \frac{a^2}{r^2}\right) + \frac{1}{2}(\sigma_H{}^* - \sigma_h{}^*)\left(1 - 4\frac{a^2}{r^2} + 3\frac{a^4}{r^4}\right)\cos 2\theta + \frac{\Delta P a^2}{r^2} \quad (1)$$

$$\sigma_{\theta\theta} = \frac{1}{2}(\sigma_H{}^* + \sigma_h{}^*)\left(1 + \frac{a^2}{r^2}\right) - \frac{1}{2}(\sigma_H{}^* - \sigma_h{}^*)\left(1 + 3\frac{a^4}{r^4}\right)\cos 2\theta - \frac{\Delta P a^2}{r^2} \quad (2)$$

$$\sigma_{r\theta} = -\frac{1}{2}(\sigma_H{}^* + \sigma_h{}^*)\left(1 + \frac{2a^2}{r^2} - 3\frac{a^4}{r^4}\right)\sin 2\theta \quad (3)$$

where, σ_{rr}, $\sigma_{\theta\theta}$ and $\sigma_{r\theta}$ are the radius, tangential, and shear stresses, respectively, acting around the borehole wall. a is the radius of the hole, r is the point of interest, θ is the angular direction measured counterclockwise from the direction of σ_H*, and ΔP is the difference between the fluid pressure in the borehole and that in the formation. Since the existence of pore water pressure is ignored in this study, $\Delta P = 0$. This well-known solution can be utilized to validate the numerical model by comparing the stress distribution around the borehole wall and along the x axis when the sample is loaded to the stage before the initiation of cracks.

In the DEM model, two sets of measurement circles (with diameter $l = 2$ mm) [*Itasca*, 2008] are installed to measure the stress state as shown in Figure 4. The first set consists of 36 measurement circles evenly located around the borehole wall with $r = 6.5$ mm. The second group is made up of 18 measurement circles located along the x axis from $x = 6.5$ mm to $x = 23.5$ mm. Stresses measured from these measurement circles can be transformed into the polar coordinate system following the equations below [*Sokolnikoff and Specht*, 1956]:

$$\sigma_{rr} = \sigma_x \cos^2\theta + \sigma_y \sin^2\theta + 2\tau_{xy}\sin\theta\cos\theta \quad (4)$$

$$\sigma_{\theta\theta} = \sigma_x \sin^2\theta + \sigma_y \cos^2\theta - 2\tau_{xy}\sin\theta\cos\theta \quad (5)$$

$$\tau_{r\theta} = (\sigma_y - \sigma_x)\sin\theta\cos\theta + \tau_{xy}(\cos^2\theta - \sin^2\theta) \quad (6)$$

where σ_x, σ_y, and τ_{xy} are the stress components measured from the measure circles. Figure 5 compares the stress distributions calculated according to the theoretical solution and that calculated according to the isotropic DEM model around the borehole wall and along the x axis when the models are loaded $\varepsilon_y = 0.08\%$

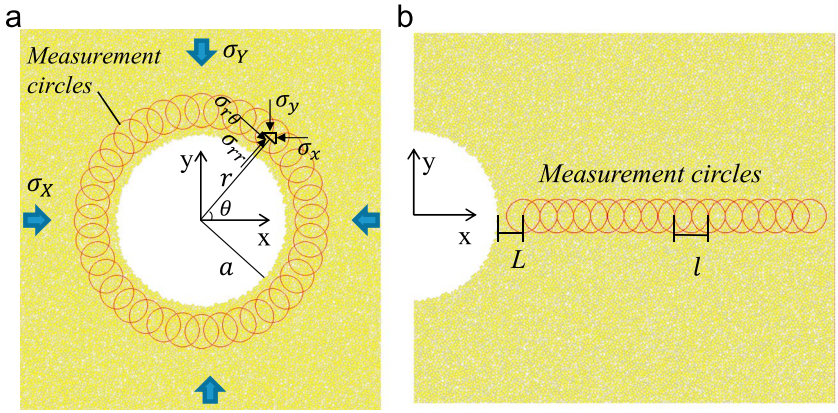

Figure 4. Location of measurement circles (a) around the borehole and (b) along the *X* axis. Diameter of the measurement circles l = 2 mm. Angle between adjacent measurement circles in the polar system is 10°. Distance between adjacent measurement circles is equal to l/2.

under various K_0. Generally, excellent agreement can be found between the DEM model and the analytical solution. Under hydrostatic stress condition ($K_0 = 1.0$), the stresses around the borehole are constant with the maximum and minimum principal stresses obtained in the tangential and radius direction, respectively. Considerable deviation of $\sigma_{\theta\theta}$ can be noticed around the borehole vicinity which may be attributed to the heterogeneity nature of DEM model. The shear stress stays constant as zero due to the symmetric geometry and loading condition. Along the *x* axis, $\sigma_{\theta\theta}$ decreases while σ_{rr} increases continuously until the two principal stresses approach to the applied far-field stress.

Significant influence of far-field stress anisotropy on the stress distribution can be noticed when $K_0 = 0.8$ and 1.25. Although the maximum principal stresses are still obtained in the tangential direction, the magnitude of $\sigma_{\theta\theta}$ fluctuates periodically with θ (Figures 5a and 5e). The maximum magnitude of $\sigma_{\theta\theta}$ arises at the same orientation with far-field minimum principal stress σ_h* ($\theta = 0°$ and 180° when $K_0 = 0.8$, while $\theta = 90°$ and 270° when $K_0 = 1.25$). Notable fluctuation of shear stress ($\sigma_{r\theta}$) can also be observed while the radius stress (σ_{rr}) stays almost constant. Slight discrepancies can also be noticed between the DEM model and analytical solution, which indicates the existence of high stress concentrations at some point due to the geometric heterogeneity resulting from packing of nonuniform-sized particles. Heterogeneity has been identified to have a significant effect on the stress distribution [*Lan et al.*, 2010] and rock strength [*Fjær and Ruistuen*, 2002]. The inhomogeneity of particle size cause rock behavior deviates from true elastic and its effect on borehole breakouts will be investigate in section 4.2 in detail.

4. Propagation of Borehole Breakouts in Isotropic Model

4.1. Borehole Breakout Under Hydrostatic Stress

Numerical test is first conducted on the isotropic model with $D = 10$ mm under monotonically increased hydrostatic stress. The vertical stress-strain curve and increment of microcracks indicate a three-stage process of breakout nucleation and growth as illustrated in Figure 6. At the initial stage, the stress-strain curve demonstrates linear elastic relationship and no microcracks occur before σ_y reaches to 41.2 MPa. After that microcracks start to increase in a steady way until σ_y approaches to a critical hydrostatic stress ($P^* = 68.2$ MPa) where the stress-strain curve shows a distinct inflection point and a sudden increase in the cumulative microcracks can be found. This critical pressure has been determined in laboratory by means of strain, acoustic emission activity, CT observations, and *P* wave velocities and amplitudes [*Dresen et al.*, 2010; *Meier et al.*, 2013] and is assumed to denote the onset of borehole breakout formation. After breakout nucleation, microcracks increase dramatically till the collapse of borehole. The borehole breakout process obtained from the DEM model under hydrostatic stress condition agree well with those observed in laboratory on sandstone [*Dresen et al.*, 2010] and shale when drilled perpendicular to beddings [*Meier et al.*, 2014, 2013; *Van den Hoek*, 2001].

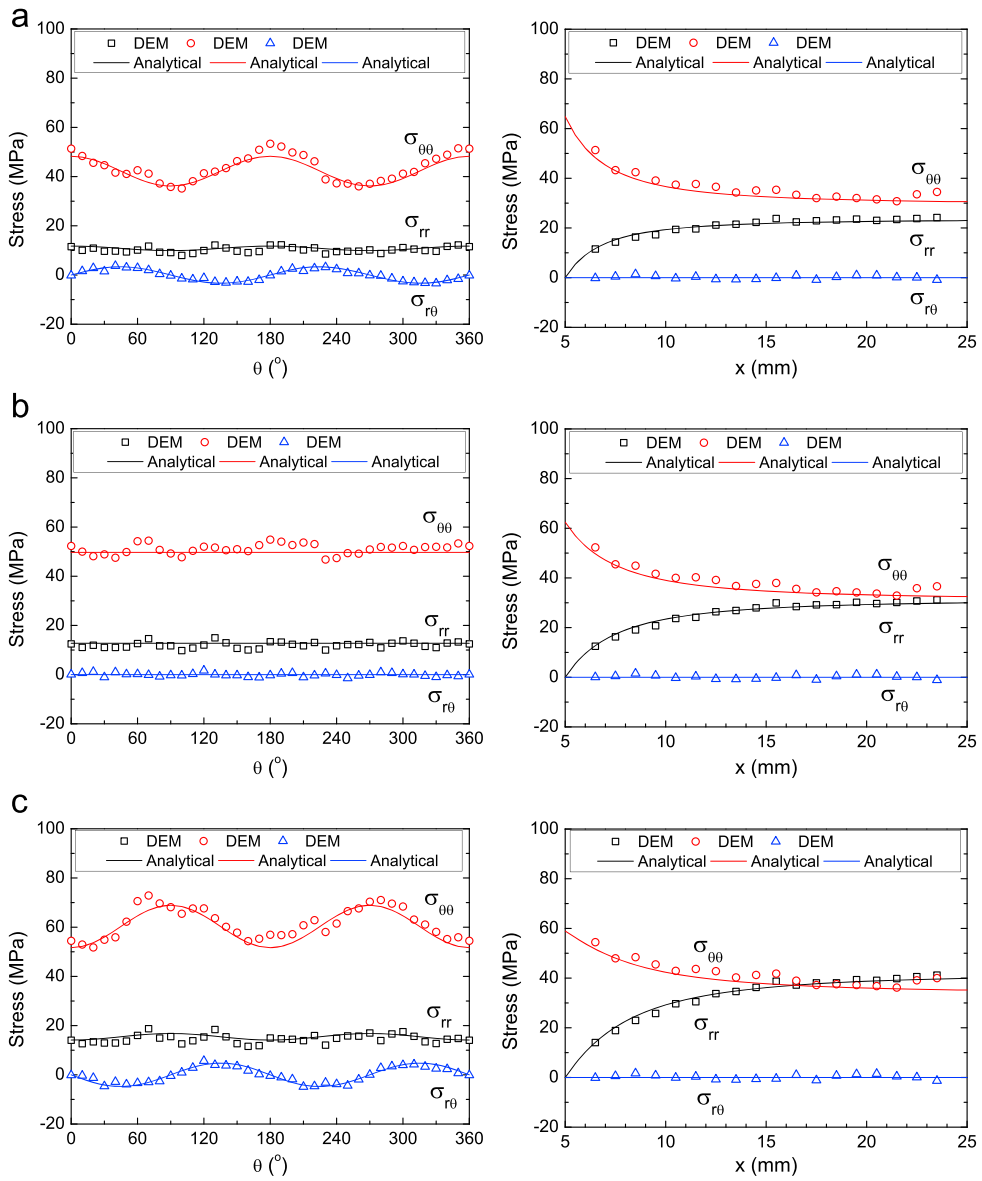

Figure 5. Comparison between stress distribution calculated from the analytical solutions and that measured from DEM model when the isotropic model is loaded to $\varepsilon_y = 0.08\%$ under different stress conditions: (a) $K_0 = 0.8$, (b) $K_0 = 1.0$, and (c) $K_0 = 1.25$. The left column show the stress around the borehole and the right column show the stress along the *X* axis.

The geometry and patterns of borehole breakouts at different loading stages are illustrated in Figure 7. The initial cracks are randomly distributed as breakout nucleates from the spots of local high stress concentration in the borehole wall. Clusters of cracks can be observed at several points around the borehole wall when $\varepsilon_y = 0.16\%$. The cracks are mainly made up of tensile failure of parallel bond which forms a shallow mesofracture penetrating into the rock in a direction subparallel to the borehole wall. As can be observed from Figure 5b, stresses at the borehole wall are mainly in the tangential direction with non to very low confining, which is close to the unconfined compression test condition, thus, compression-induced tensile cracks can develop. As the applied far-field stress increases, more fractures emerge and head back for the surface of borehole wall in a direction conjugate to the initial propagation. Breakout consistently grows along the borehole wall and also propagates in a radial direction. With increase in depth, four V-shaped major symmetric breakouts arise when $\varepsilon_y = 0.24\%$ with depth of about half of borehole radius. After that the breakouts seem to be in an unfavorable position for further growth of failure and secondary fractures start to propagate from

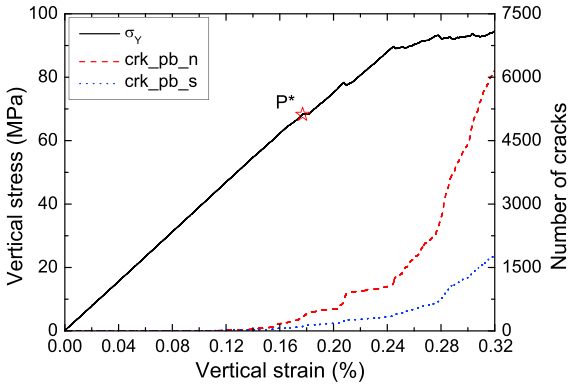

Figure 6. Stress-strain curve and the increment of microcracks for the isotropic model with $D = 10$ mm under hydrostatic stress condition ($K_0 = 1$). P^* represents the critical hydrostatic stress where the stress-strain curve shows a distinct inflection point.

the tips of these fractures which ultimately result in spiral-shaped shear fractures around the borehole. Evolution of the geometry and patterns of the breakouts is in excellent agreement with previous failure modes observed on shale [*Meier et al.*, 2013] and other rock formations [*Van den Hoek*, 2001] when hydrostatic far-field stress conditions are applied.

4.2. Effect of Particle Size Distribution

To elucidate how particle-scale geometric heterogeneity influences the development of borehole breakout, two more models with different size distributions ($R_{max}/R_{min} = 1.40$ and 1.80) are constructed and tested. In all of these simulations, particle size satisfies a uniform distribution with the medium particle size fixed as $R_{50} = 0.1$ mm so that different models have the similar resolution (number of particles cross the borehole diameter). In order to only look at the effect of particle size distribution, the same particle and parallel bond properties calibrated in section 3.1 are assigned to all models. Uniaxial compression tests conducted on these models characterize similar mechanical properties as listed in Table 2. The errors between them are within 10% with the most notable impact of microgeometric heterogeneity found on the peak strength.

Significant influence of the particle size distribution can be found on the propagation and geometry of borehole breakouts. The critical pressure (P^*) increases from 66.6 MPa when $R_{max}/R_{min} = 1.40$ to 76.6 MPa when $R_{max}/R_{min} = 1.80$. Most importantly, different failure patterns of borehole breakouts develop in samples with

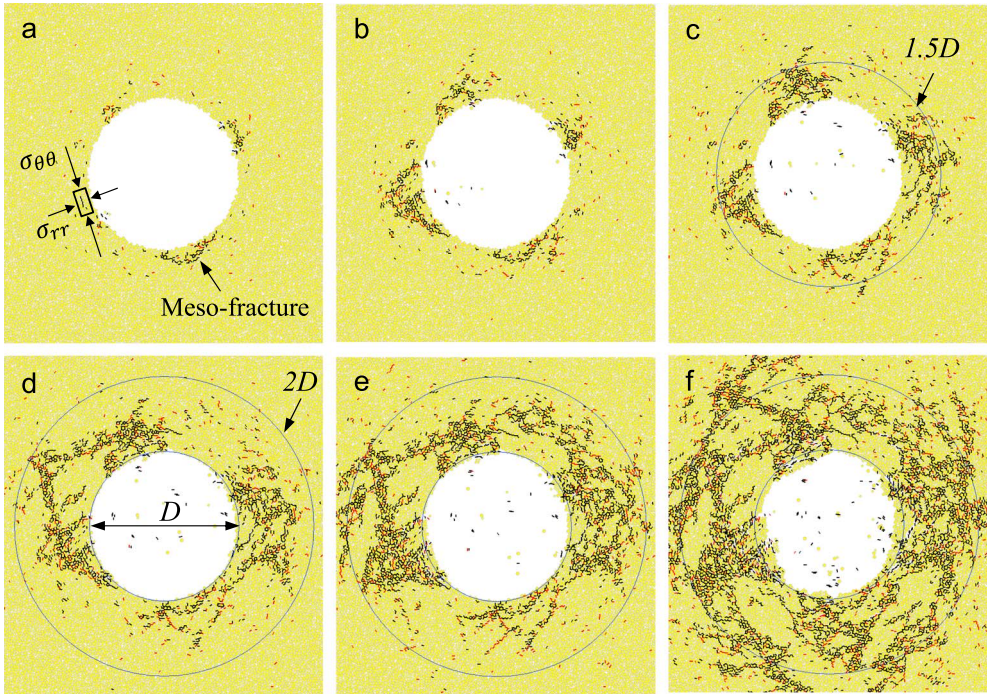

Figure 7. Propagation of borehole breakout under hydrostatic stress condition: (a) $\varepsilon_y = 0.16\%$, (b) $\varepsilon_y = 0.20\%$, (c) $\varepsilon_y = 0.24\%$, (d) $\varepsilon_y = 0.26\%$, (e) $\varepsilon_y = 0.28\%$, and (f) $\varepsilon_y = 0.32\%$ (Black lines represent tensile failure of parallel bond; red lines represent shear failure of parallel bond.)

Table 2. Mechanical Responses Obtained From Uniaxial Compression Tests Conducted on Samples With Different Particle Size Distributions[a]

Particle Size Distribution (R_{max}/R_{min})	Number of Particles	Uniaxial Compression Strength, UCS (MPa)	Young's Modulus, E (GPa)	Poisson's Ratio
1.4	71,493	78.97	28.08	0.24
1.66	71,275	74.85	27.52	0.24
1.8	70,981	76.29	27.55	0.24

[a]Uniaxial compression tests are conducted on samples with size 50 mm × 25 mm.

different particle size distributions under hydrostatic stress conditions as shown in Figure 8. Spiral-shaped shear fractures preferentially develop in an assembly that has a relatively uniform particle size distribution ($R_{max}/R_{min} = 1.40$) which can be noted in Figure 8a. Similar patterns have been observed in laboratory hollow cylinder tests on Posidonia shale drilled perpendicular to beddings as shown in Figure 8c [*Meier et al*., 2013]. In contrast, in a more heterogeneous system ($R_{max}/R_{min} = 1.80$), localized concentration of cracks typically occurs at three locations around the borehole wall roughly 120° from each other as illustrated in Figure 8b. The breakouts are nearly identical to these observed in Cordova Cream and St. Meinrad sandstone (Figure 8d) as far as their number and orientation when the two horizontal principal stresses are equal [*Haimson*, 2007]. These differences can be attributed to microstructural heterogeneities as local stress perturbations that result from grain-shaped heterogeneity was found to have large effect on macroscopic properties [*Lan et al*., 2010]. Distribution of major principal stress ($\sigma_{\theta\theta}$) around the borehole wall when

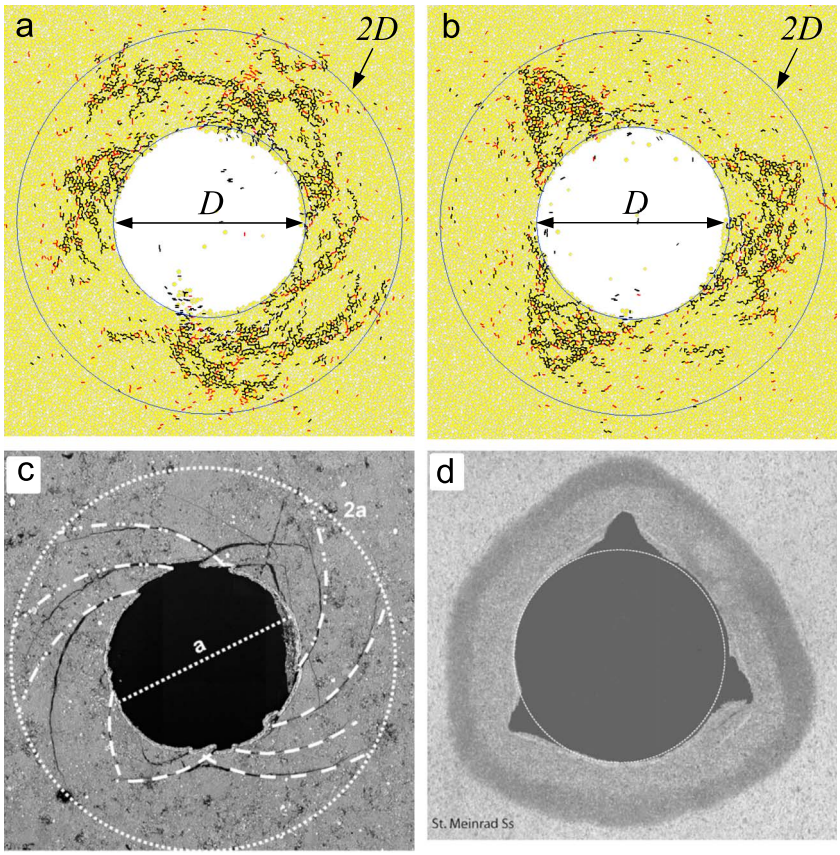

Figure 8. Distribution of microcracks when the model with (a) $R_{max}/R_{min} = 1.40$ loaded to $\varepsilon_y = 0.24\%$ and (b) $R_{max}/R_{min} = 1.80$ loaded to $\varepsilon_y = 0.26\%$ (black lines represent tensile failure of parallel bond; red lines represent shear failure of parallel bond) and the observations from laboratory tests: (c) Borehole breakout of hydrostatically loaded Posidonia shale [*Meier et al*., 2013] and (d) Borehole breakouts of the St. Meinrad sandstone when $\sigma_H = \sigma_h = 60$ MPa [*Haimson*, 2007].

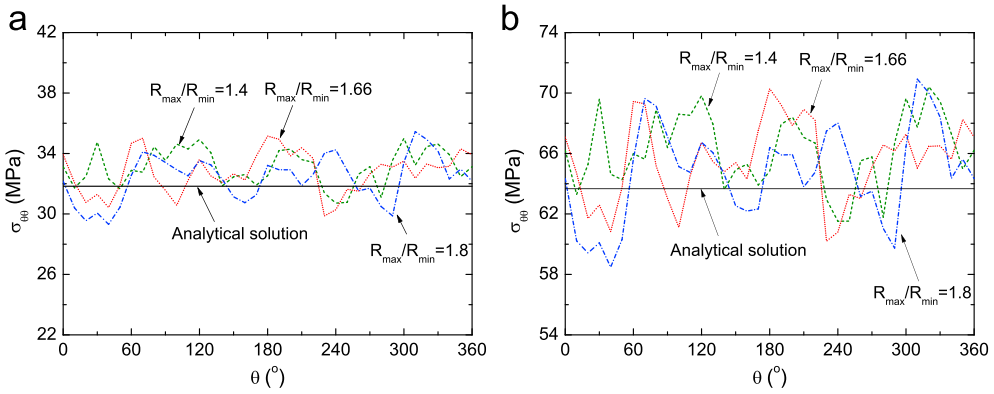

Figure 9. Variation of maximum principal stress ($\sigma_{\theta\theta}$) versus θ measured from the numerical model with various particle size distribution (R_{max}/R_{min} = 1.4, 1.66, and 1.8) when loaded to (a) $\sigma_Y = \sigma_X = 20$ MPa and (b) $\sigma_Y = \sigma_X = 40$ MPa together with the analytical solutions (solid line).

$\sigma_Y = \sigma_X = 20$ MPa and 40 MPa is compared in Figures 9a and 9b, respectively. The distribution of $\sigma_{\theta\theta}$ is more fluctuated around the borehole wall in the relatively heterogeneous model than that in the homogeneous model. The concentration of stress may cause localization of microcracks and ultimately lead to the different failure patterns of borehole breakout discussed above.

4.3. Effect of Borehole Diameter

Size effect on the borehole breakouts is investigated in this section by performing numerical tests on samples with D that vary from 2 mm to 16 mm. A total of eight tests are conducted under hydrostatic stress condition. A significant decrease of the critical pressure (P^*) required to nucleate breakouts with increasing borehole diameter can be observed as summarized in Figure 10a. At the critical hydrostatic pressure P^*, the maximum principal stress exists in the tangential direction

$$\sigma_{\theta\theta} = P^* \times \frac{b^2}{b^2 - a^2} \times \left(1 + \frac{a^2}{r^2}\right) \tag{7}$$

The minimum principal stress is obtained in the radial direction

$$\sigma_{rr} = P^* \times \frac{b^2}{b^2 - a^2} \times \left(1 - \frac{a^2}{r^2}\right) \tag{8}$$

where b is half of the specimen length (25 mm) in this study. The uniaxial compression strength (UCS) normalized critical tangential stresses are plotted in Figure 10b versus borehole diameter. A similar trend is observed

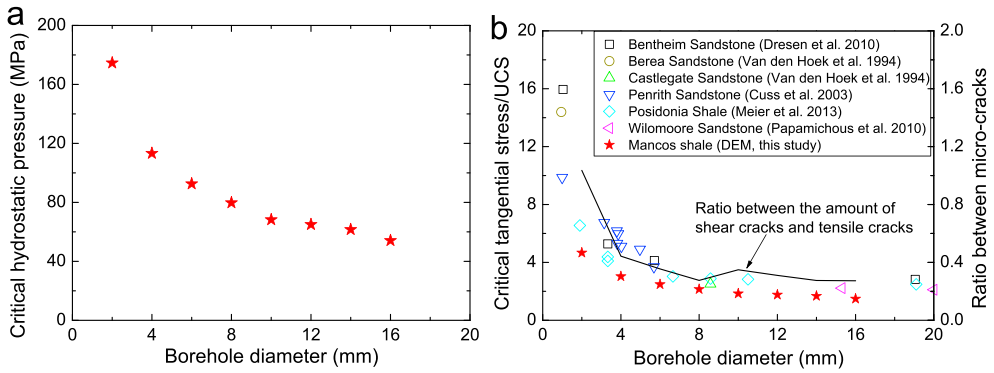

Figure 10. Effect of borehole diameter. (a) Reduction of the critical hydrostatic pressure P^* for borehole breakout initiation. (b) UCS-normalized critical tangential stress at the borehole wall for breakout nucleation and the corresponding ration between shear cracks and tensile cracks versus borehole diameter.

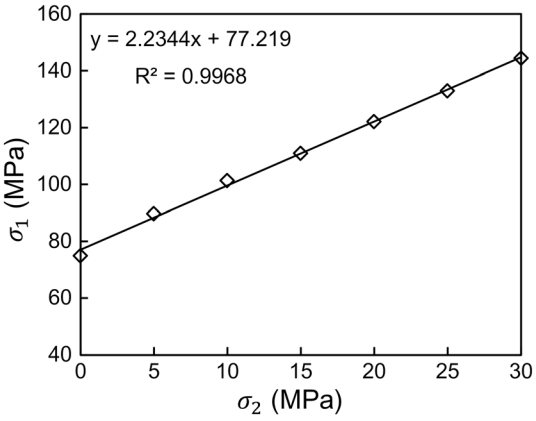

Figure 11. Variation of peak strength versus confining pressures obtained from confined compression tests and curve-fitted failure criterion.

between the numerical model and experimental results from various rock types [*Cuss et al.*, 2003; *Dresen et al.*, 2010; *Ewy and Cook*, 1990a; *Meier et al.*, 2013; *Papamichos et al.*, 2010; *Van den Hoek et al.*, 1994]. Another phenomenon worth noting is the transformation of microcrack modes with the reduction of borehole diameter. The ratio between shear failures to tensile failure of parallel bond at critical hydrostatic pressure is plotted in Figure 10b, which corresponds well with the trend of normalized critical tangential stress. The scale effect may partly be related to different failure mechanisms involved in breakout formation as our previous studies on failure process of brittle rocks have confirmed that the ratio between shear failure and tensile failure increases with the increase of confining pressure [*Duan et al.*, 2015b].

A series of confined compression tests (confining pressure $\sigma_2 = 5$, 10, 15, 20, 25, and 30 MPa) are conducted on the numerical model used for calibration. Figure 11 presents the variation of peak strength which can be described by the following criterion:

$$\sigma_{1,\text{peak}} = 2.2344 \times \sigma_2 + 77.219 \quad \left(R^2 = 0.9968\right) \tag{9}$$

where $\sigma_{1,\text{peak}}$ is the peak strength under confining pressure σ_2. By inserting equations (7) and (8) into the failure criterion (equation (9)), the relationship between P^*, borehole diameter (a), sample size (b), and point of breakout nucleation (r^*) can be described as follows:

$$P^* = 77.219 \times \frac{b^2 - a^2}{b^2} \times \left(\frac{(r^*)^2}{3.2344 \times a^2 - 1.2344 \times (r^*)^2} \right) \tag{10}$$

From equation (10), the location of breakout nucleation (r^*) at critical pressure (P^*) can be calculated as listed in Table 3. Figure 12 illustrates the distribution of microcracks before and after P^* when $D = 2$, 8, and 16 mm, respectively. For large boreholes ($D = 8$ mm and 16 mm), breakouts nucleate from the boundary of circles defined by r^* calculated from equation (10) with mechanism dominantly extensile cracking. When the borehole is small ($D = 2$ mm), an overestimation of the size effect can be found as breakouts exceed the calculated range and are strongly distorted on the sides when the fractures initiate (Figures 12a and 12d). This might be attributed to the fact that for small borehole, the critical tangential pressure ($\sigma_{\theta\theta}$ at critical hydrostatic stress stage) seems to approach the grain-crushing pressure in reality [*Meier et al.*, 2013; *Zhang et al.*, 1990], whereas the mechanism is missing in the numerical model.

Table 3. Location of Borehole Breakout Nucleation Point Calculated From Analytical Solution-Based Failure Criterion Obtained From DEM Simulations

D (mm)[a]	a (mm)[b]	b (mm)[c]	r^* (mm)[d]
2	1	25	1.39
4	2	25	2.60
6	3	25	3.75
8	4	25	4.85
10	5	25	5.90
12	6	25	7.00
14	7	25	8.15
16	8	25	9.00

[a] D: borehole diameter.
[b] a: borehole radius.
[c] b: width of specimen.
[d] r^*: distance from point of breakout nucleation to borehole center.

4.4. Effect of Far-Field Stress Anisotropy

Numerical tests with $K_0 = 0.8$ and 1.25 are performed on the isotropic model with $D = 10$ mm to study the effect of far-field stress anisotropy. Stress-strain curves and increments of microcracks are illustrated in Figures 13a and 13b, respectively.

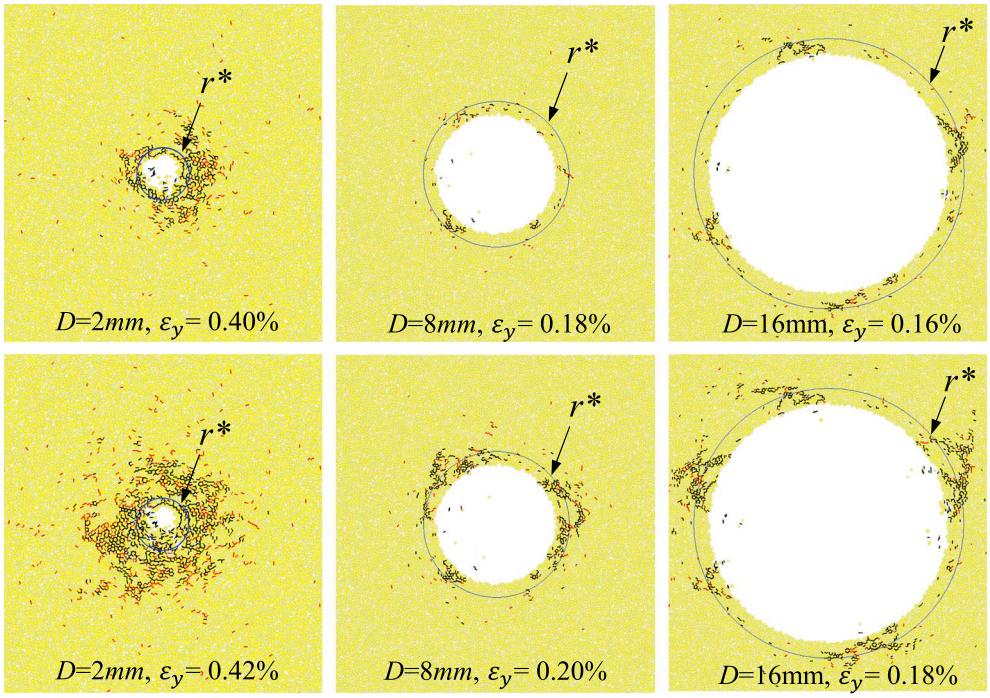

Figure 12. Distribution of microcracks (top row) before and (bottom row) after the critical tangential stress (P^*) when the borehole diameter $D = 2$, 8, and 16 mm. Red short lines represent the shear failure of parallel bond; black short lines represent the tensile failure of parallel bond. The solid circles represent the range of damage zone at critical tangential stress calculated from the analytical solutions (with radius of r^*).

Different from the spiral-shaped, relatively rounded breakout obtained under hydrostatic stress, significant effect of far-field stress anisotropy can be observed from Figures 13c–13f. At the critical stage (Figures 13c and 13d), tensile cracks behind the borehole in two zones aligned with σ_H proceed the development of breakouts which display two V-shaped fractures on the opposite direction across the diameter along the minimum principal stress direction (x direction when $K_0 = 0.8$ and y direction when $K_0 = 1.25$). In some cases, damage at the tip of the bands involves grain crushing which ultimately results in slot-like fracture band with the aid of washing out in porous sandstones [*Haimson*, 2007; *Haimson and Lee*, 2004; *Katsman et al*., 2009]. The mechanisms have been studied with the introduction of particle breakage algorithms [*Katsman et al*., 2009; *Katsman and Haimson*, 2011; *Lee et al*., 2015] which is beyond the scope of our study. With the increasing of far-field stresses, the associated disturbance of the local stress field initiates new fractures in front of the breakout tip which results in dog ear-type breakouts form by continuously extending the breakout to a deeper depth and wider span approximately similar to the initial borehole radius. The sequential spalling of rock from the borehole wall results in episodic growth of breakouts and ultimately leads to two symmetric V-shaped breakouts on opposite sides of the borehole along the minimum far-field principal stress springline (Figures 13e and 13f). The simulated stress-induced borehole breakout pattern is in good agreement with the observations in laboratory (Figure 13g) [*Addis et al*., 1990; *Lee and Haimson*, 1993]. Therefore, the numerical model can be applied in the future investigation of the relationship between borehole breakout shape and size with the direction and magnitude of in situ stress [*Haimson and Song*, 1993; *Vernik and Zoback*, 1992; *Zoback et al*., 2003, 1985].

5. Propagation of Borehole Breakouts in Anisotropic Model

5.1. Effect of Rock Anisotropy on the Stress Distribution

Stress distributions measured from the isotropic and anisotropic models under three far-field stress conditions: (a) $\sigma_X = 16$ MPa, $\sigma_Y = 20$ MPa; (b) $\sigma_X = 20$ MPa, $\sigma_Y = 20$ MPa; and (c) $\sigma_X = 25$ MPa, $\sigma_Y = 20$ MPa are compared with the analytical solutions calculated form equations (1)–(3). One can tell from Figure 14 that the existence of beddings significantly alters the stress distribution around borehole compared with conditions in isotropic model. Significant fluctuation of $\sigma_{\theta\theta}$ and $\sigma_{r\theta}$ can be observed on the anisotropic model. Under

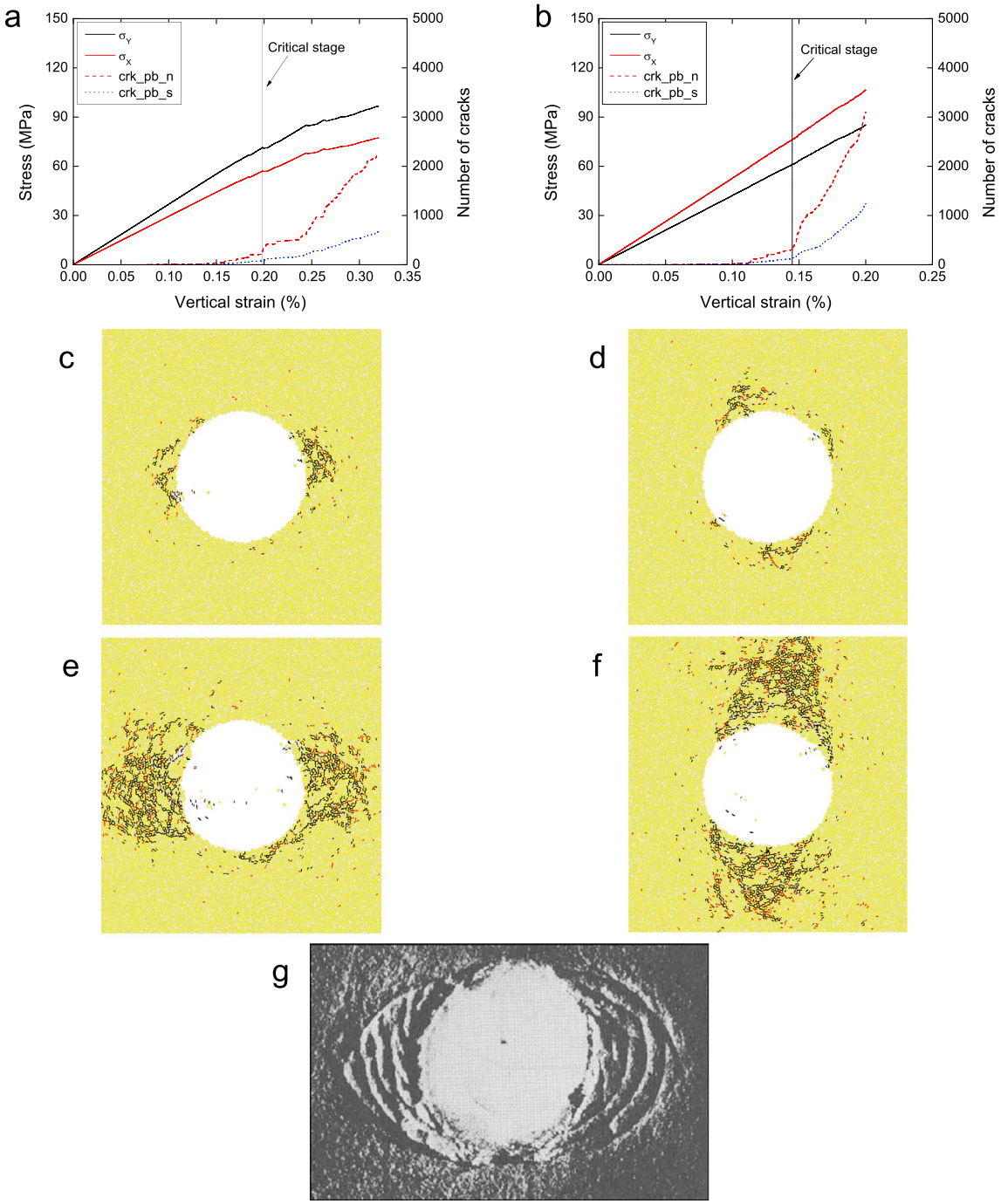

Figure 13. Influence of far-field stress anisotropy. Stress-strain curve and increment of microcracks when (a) $K_0 = 0.8$ and (b) $K_0 = 1.25$. The distribution of microcracks when (c) $K_0 = 0.8$, $\varepsilon_y = 0.20\%$; (d) $K_0 = 1.25$, $\varepsilon_y = 0.14\%$; (e) $K_0 = 0.8$, $\varepsilon_y = 0.30\%$; and (f) $K_0 = 1.25$, $\varepsilon_y = 0.18\%$. Red short lines represent the shear failure of parallel bond; black short lines represent the tensile failure of parallel bond. (g) Wellbore breakouts in homogeneous rocks from laboratory test [*Addis et al.*, 1990], from *Zhang* [2013].

hydrostatic stress (Figure 14c), the maximum $\sigma_{\theta\theta}$ arises when θ is around 130° and 320° with the magnitude of 39.3 MPa, which exceeds 24% of the value calculated from equation (1) (31.8 MPa). Under anisotropic far-field stresses, both the magnitude and the orientation of the maximum $\sigma_{\theta\theta}$ differ from the isotropic model. When $K_0 = 0.8$, the maximum $\sigma_{\theta\theta}$ emerges around $\theta = 170°$ and 340° with the magnitude of 38.5 MPa, apparently higher than the isotropic case ($\sigma_{\theta\theta} = 32.8$ MPa when $\theta = 0°$ and 180°). When $K_0 = 1.25$, the maximum $\sigma_{\theta\theta}$ is obtained at $\theta = 120°$ and 290° with the maximum $\sigma_{\theta\theta} = 47$ MPa, which is 14.6% higher than the isotropic model (41 MPa when $\theta = 90°$ and 270°).

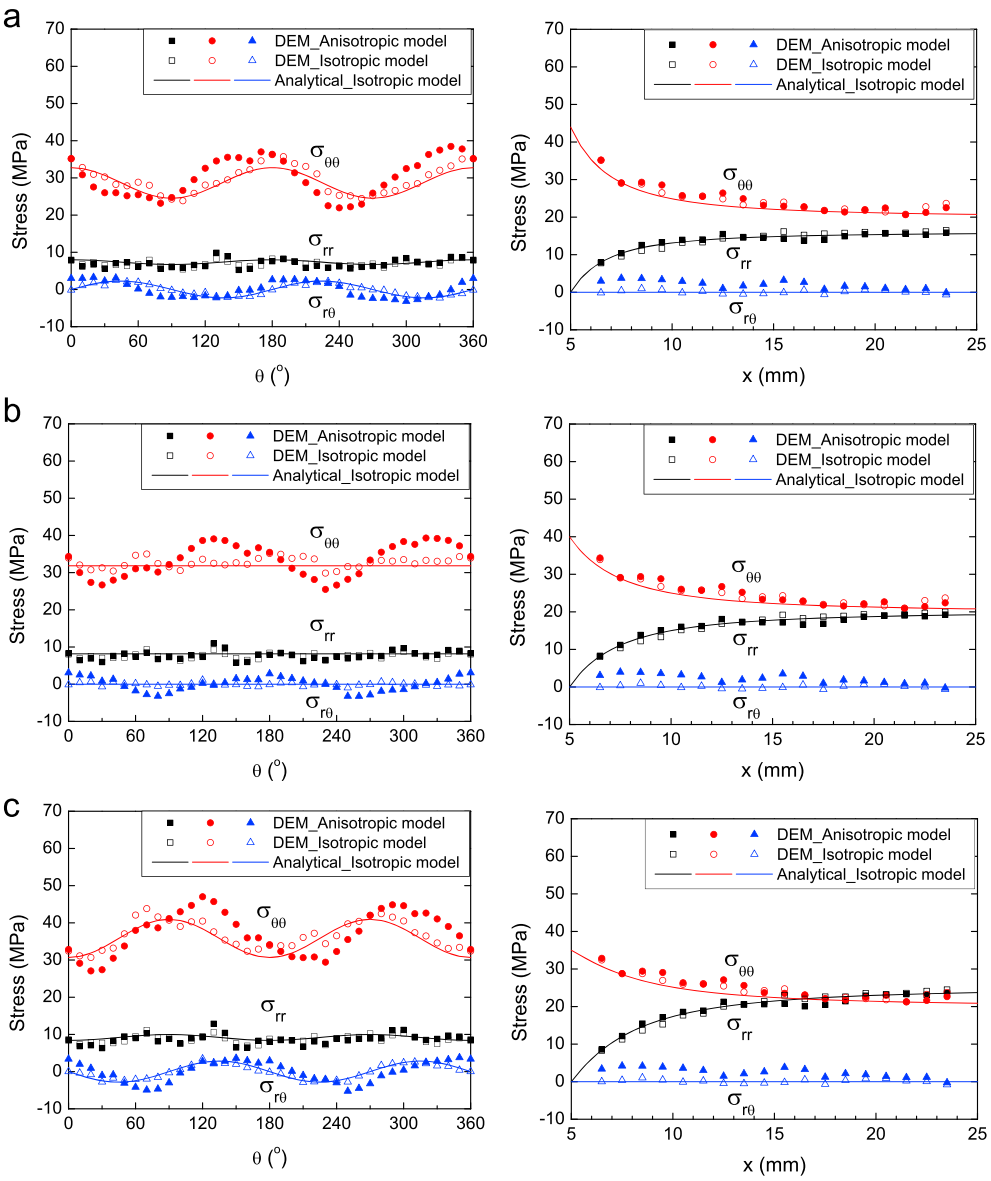

Figure 14. Comparison between stress distributions around borehole (left column) and along *X* axis (right column) measured from anisotropic DEM model, isotropic DEM model and calculated from isotropic analytical solutions under different far-field stress conditions: (a) $\sigma_X = 16$ MPa, $\sigma_Y = 20$ MPa; (b) $\sigma_X = 20$ MPa, $\sigma_Y = 20$ MPa, and (c) $\sigma_X = 25$ MPa, $\sigma_Y = 20$ MPa.

Variations of $\sigma_{\theta\theta}$ measured from anisotropic models versus θ are directly compared in Figure 15a. As same σ_Y is applied, tangential stress along the *y* direction ($\theta = 0°$ and 180°) is equivalent for the three cases. Far-field stress anisotropy leads to the deviation of maximum principal stress orientation which becomes closer to the direction of minimum principal stress applied in the far field.

In the study of *Fjær and Nes* [2014], a modified "plane of weakness model" was found to give a better representation of the anisotropic strength of the Mancos outcrop shale. This failure criterion consists of the criterion for inherent failure and the criterion for failure along a weak plane as given in equations (11) and (12), respectively

$$\mathrm{UCS} = \frac{2S_0\cos\phi\left(1-\eta\sin^2 2\beta\right)}{1-\sin\phi}, \quad \text{when} \quad \beta < 45° \ \text{ or } \ \beta > 71° \tag{11}$$

$$\mathrm{UCS} = \frac{2S_{0w}\cos\phi_w\left(1-\eta\sin^2 2\beta\right)}{\sin 2\beta\cos\phi_w - (\cos 2\beta + 1)\sin\phi_w}, \quad \text{when} \quad 45° < \beta < 71° \tag{12}$$

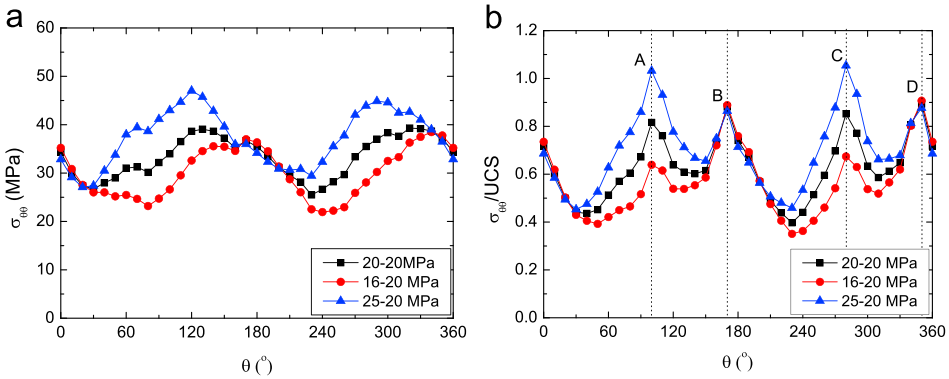

Figure 15. (a) Variation of tangential stress ($\sigma_{\theta\theta}$) versus the orientation when the far-field stress conditions (σ_X-σ_Y) are 20 MPa to 20 MPa, 16 MPa to 20 MPa, and 25 MPa to 20 MPa. (b) The UCS-normalized tangential stress as a function of orientation.

where S_0 is the inherent cohesion, ϕ is the corresponding friction angle, η is a free parameter which can be determined experimentally, and S_{0w} and ϕ_w are the cohesion and corresponding friction angle of the weak planes, respectively. Parameters determined by *Fjær and Nes* [2014] in laboratory are adopted, and the UCS-normalized major principal stress is given in Figure 15b. Different from the bimodal curve of tangential stress, four crests can be identified on the normalized maximum principle stress, in which direction wellbore breakouts are more likely to initiate. Of course, the above analysis is an inevitable coarse estimation due to the ignorance of minimum principal stress and the fact that failure strength is a function not only of loading direction but also of confinement [*Niandou et al*., 1997]. Properly accounting for the orientation- and confining-dependent strength of shales can be critical for the successful design of drilling high-inclined wells [*Lee et al*., 2012; *Ong and Roegiers*, 1993; *Zhang*, 2013].

5.2. Evolution of Borehole Breakout in Anisotropic Model

The stress-strain relationship and the increment of microcracks for the anisotropic model under hydrostatic stress are illustrated in Figure 16, from which three distinct stages can also be identified. No microcracks occur at the initial linear elastic stage until σ_y reaches to 20 MPa. After that shear failure of smooth joint starts to occur and increase in a slow and steady manner. The stress-strain curve maintains linear until σ_y approaches to the critical hydrostatic stress (P^* = 49.9 MPa). During this stage, tensile failure of parallel bond starts to arise but takes a small proportion. After σ_y exceeds P^*, the stress-strain curve deviates from linear elastic and more tensile failure of parallel bond emerges in a dramatic way until the collapse of wellbore. The critical pressure (P^*) decreases from 68.2 MPa to 49.9 MPa when borehole orientated parallel with beddings, which is about 73% of the value when borehole is drilled perpendicular with weak layers. This result is consistent with the results in laboratory conducted by *Meier et al*. [2014] on Posidal shale and provides numerical evidence for the field observation that borehole instability problems were experienced when drilling parallel or with small angle between bedding direction in which the breakout initiation is lower [*Okland and Cook*, 1998].

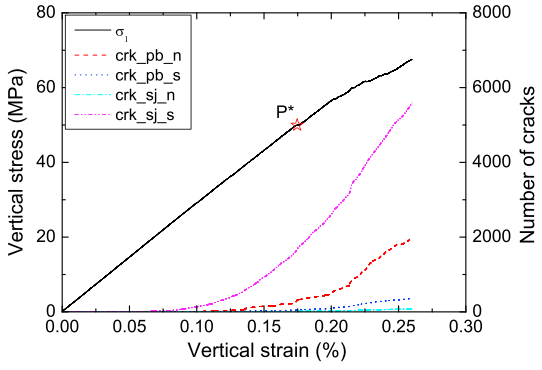

Figure 16. Stress-strain curve and increment of microcracks for anisotropic case (β = 45°) under hydrostatic stress condition (K_0 = 1).

Distributions of microcracks at various loading stages are illustrated in Figure 17. Initially, excessive shear loading along the bedding planes in the tangential orientations to the borehole leads to the initiation of shear failure of smooth joint, nucleating and growing along bedding planes approximately tangential to the borehole wall (ε_y = 0.12%). These cracks around the

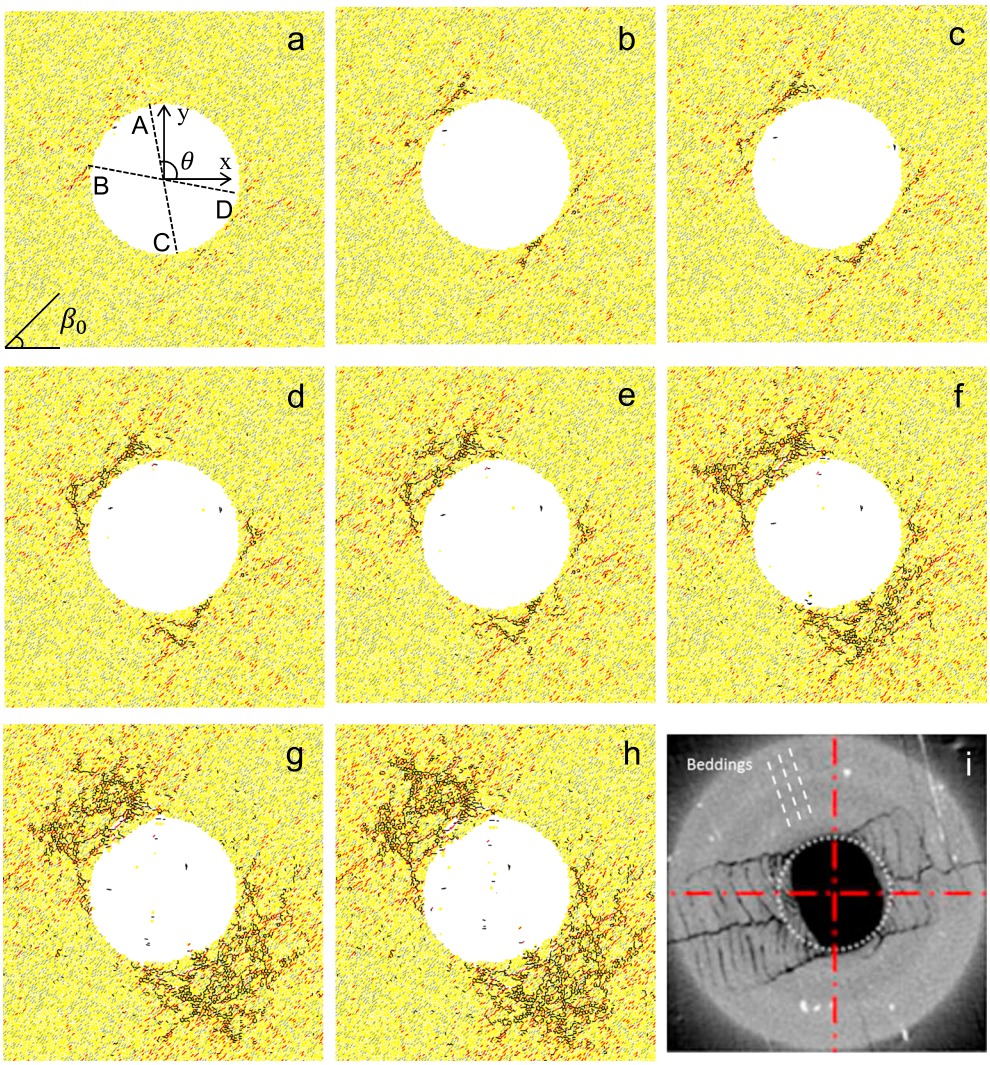

Figure 17. Propagation of borehole breakouts in anisotropic model under hydrostatic stress ($K_0 = 1$) condition: (a) $\varepsilon_y = 0.12\%$, (b) $\varepsilon_y = 0.14\%$, (c) $\varepsilon_y = 0.16\%$, (d) $\varepsilon_y = 0.18\%$, (e) $\varepsilon_y = 0.20\%$, (f) $\varepsilon_y = 0.22\%$, (g) $\varepsilon_y = 0.24\%$, and (h) $\varepsilon_y = 0.26\%$. Blue lines represent the weak layers; red lines represent failure of smooth joint; black lines represent failure of parallel bond. (i) High-resolution XRCT scan of the central part of the Opalinus Clay hollow specimen cored parallel to the bedding planes [after *Labiouse and Vietor*, 2014]. Dash lines represent the beddings.

borehole serve as starting points for more severe breakouts forming as buckling failure. Propagation of these shear failures gives rise to the occurrence of tensile failure of parallel bond, which initiates from their tips and propagates in the direction perpendicular to the weak layers due to the tensile stress field induced by bedding slippage (Figures 17b and 17c) [*Amann et al.*, 2011; *Duan et al.*, 2015a; *Rawling et al.*, 2002]. The interaction between the shear failure of smooth joint and tensile failure of parallel bond results in a four-lobed breakout pattern (Figure 17d). The locations of the four corners are consistent with the four crests marked in Figure 15b. Cracks subparallel to the bedding planes open and lead to a buckling failure in two regions that extend from the borehole in the direction normal to bedding (Figures 17e–17h). The width of the damaged region is similar to the diameter of the borehole. The borehole breakout shape agrees well with that observed in laboratory on hollow cylinder tests on Opalinus Clay [*Labiouse and Vietor*, 2014] and Posidonia shale [*Meier et al.*, 2014], as well as the observations obtained in field test on small holes [*Kupferschmied et al.*, 2015; *Labiouse and Vietor*, 2014].

5.3. Effect of Far-Field Stress Anisotropy

Numerical tests on the anisotropic model with $K_0 = 0.8$, and 1.25 are conducted to evaluate the effect of far-field stress anisotropy on the breakout process and pattern when wellbore cored parallel with beddings.

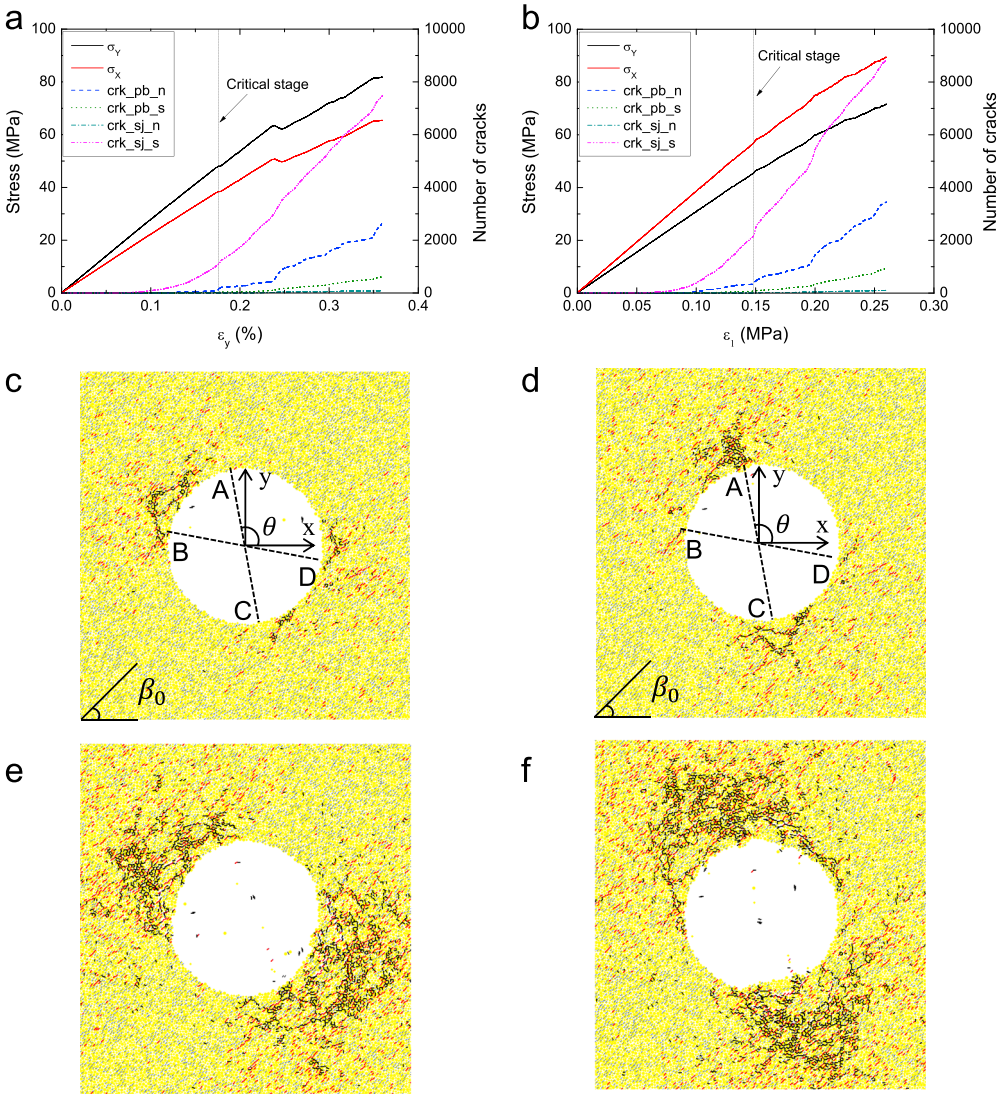

Figure 18. Effect of stress anisotropy on the evolution of borehole breakout in anisotropic rock formation. Stress-strain curve and increment of microcracks when (a) $K_0 = 0.8$ and (b) $K_0 = 1.25$. Distribution of microcracks when (c) $K_0 = 0.8$, $\varepsilon_y = 0.18\%$; (d) $K_0 = 1.25$, $\varepsilon_y = 0.14\%$; (e) $K_0 = 0.8$, $\varepsilon_y = 0.30\%$, and (f) $K_0 = 1.25$, $\varepsilon_y = 0.22\%$. Blue lines represent the weak layers; red lines represent failure of smooth joint; black lines represent failure of parallel bond.

Same with previous cases, the fracture process can be divided into three stages (see Figures 18a and 18b): linear elastic stage with none microcracks, linear elastic stage with steady increased cracks, and unstable stage with dramatic development of cracks. Distributions of microcracks before and after the critical stage are illustrated in Figures 18c–18f. For the anisotropic rock formation, the shape and orientation of the breakouts are still bedding dominated, but apparent influence of far-field stress condition can be noticed. Distinct difference between the onset of borehole breakout can be found in Figures 18c and 18d, namely, under anisotropic far-field stress, concentration of microcracks arises in zones B and D when $K_0 = 0.8$ and in zones A and C when $K_0 = 1.25$. These phenomena are in excellent agreement with the variation of UCS-normalized maximum principal stress as shown in Figure 15b. With the ongoing of tests, fractures generally propagate in the direction perpendicular to the bedding but still rotate slightly to the direction of minimum principal stress (σ_x when $K_0 = 0.8$ and σ_y when $K_0 = 1.25$). The percentage of microcracks at failure stage within different orientations is plotted in Figure 19 for the anisotropic model with various $K_0 = 0.8$, 1.0, and 1.25. Significant effect of the far-field stress anisotropy can be identified.

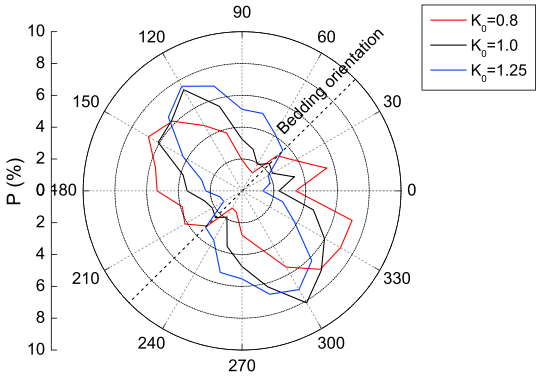

Figure 19. Orientation distribution of microcracks at the failure stage ($\varepsilon_y = 0.3\%$ when $K_0 = 0.8$, $\varepsilon_y = 0.26\%$ when $K_0 = 1.0$, $\varepsilon_y = 0.22\%$ when $K_0 = 1.25$) from the anisotropic model loaded with different far-field stress ratios.

6. Discussion

In this study, DEM model is generated to investigate the borehole breakout observed in laboratory at reduced scale, which does not have the dimension of a real borehole. The selection of particle size is optimized with regard to the balance between the representativeness of calculation results and the computational burden.

According to the study of *Potyondy and Cundall* [2004], the elastic constants of PFC2D models appear to be independent of particle size by scaling the parallel bond stiffness ($\overline{k}^n$ and $\overline{k}^s$) as a function of particle size via the following equations:

$$k_n = 2tE_c, t = 1 \tag{13}$$

$$k_s = k_n(k_n/k_s) \tag{14}$$

$$\overline{k}^n = \frac{\overline{E}_c}{R^{(A)}} + R^{(B)} \tag{15}$$

$$\overline{k}^s = \overline{k}^n\left(\overline{k}^n/\overline{k}^s\right) \tag{16}$$

where R is particle radius and E_c and $\bar{E}_c$ are the Young's modulus of the particle and cement, respectively. k_n/k_s and $\overline{k}^n/\overline{k}^s$ are the ratios of normal to shear stiffness of the particles and cements, respectively. Mechanical properties obtained from uniaxial compression tests conducted on samples with different particle sizes are illustrated in Table 4. Both our simulation results (see Tables 2 and 4) and previous studies [*Ding et al.*, 2014; *Koyama and Jing*, 2007; *Potyondy and Cundall*, 2004] confirm that the effect of particle size on the macroscopic responses under uniaxial compression test is not significant as long as the resolution is high enough, namely, there is no constant increase or decrease trend.

For the borehole breakout problem, effect of particle size is examined by conducting two more series of numerical simulations with different particle sizes, in which particle size follow the same uniform distribution with $R_{max}/R_{min} = 1.66$ and $R_{min} = 0.15$ and 0.2 mm, respectively. All the numerical samples have the same size (50 mm × 50 mm), and borehole diameter (D) varies from 4 mm to 16 mm. The same microparameters as listed in Table 1 are assigned to the particles and parallel bonds for all of the models. Simulations conducted on the numerical models demonstrate the same effect of borehole diameter as illustrated in Figure 20, that is, a significant decrease of the critical pressure (P^*) required to nucleate breakouts with increasing borehole diameter. Therefore, the borehole diameter effect is an emergent property of the DEM model which is independent of selection of the particle size. Theoretically, borehole breakouts observed in the DEM model can represent the breakouts observed in the field when the sample size and particle size are enlarged. In practice, the length and spacing of weak layers inserted into the DEM model should be linked to the scale of bedding observed in field in the study of field problem.

Table 4. Mechanical Properties Obtained From Uniaxial Compression Tests Conducted on DEM Model With Different Particle Sizes (Sample Size 50 × 25 mm, Particle Size Follow the Uniform Distribution With $R_{max}/R_{min} = 1.66$ and $R_{min} = 0.075$, 0.15, and 0.2 mm, Respectively)

Cases	R_{min} (mm)	UCS (MPa)	Young's modulus (GPa)	Poisson's Ratio
1	0.075	74.85	27.52	0.243
2	0.15	79.72	27.54	0.247
3	0.2	76.13	27.10	0.241

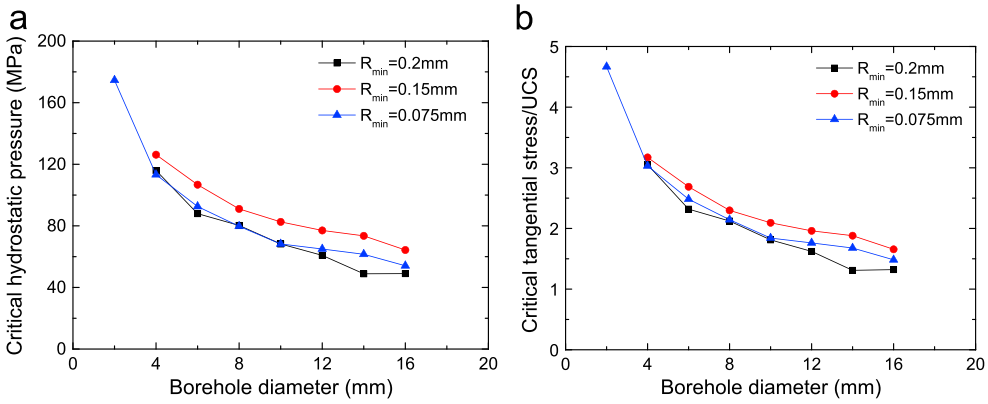

Figure 20. (a) Critical hydrostatic pressure and (b) UCS-normalized critical tangential stress ($\sigma_{\theta\theta}$) at the borehole wall for breakout nucleation measured from samples with different particle size (R_{min}). The sample size is 50 mm × 50 mm. Particle size follow the same uniform size distribution with $R_{max}/R_{min} = 1.66$ and bounded by $R_{min} = 0.2$, 0.15 and 0.075 mm, respectively.

7. Conclusions

The evolution of stress-induced borehole breakouts in intact anisotropic rock is investigated in this study based on the DEM modeling. The microstructure of sedimentary rock is explicitly represented by inserting a series of parallel smooth joint contacts into the bonded particles. The numerical model can reproduce both the strength and deformation characteristics of Mancos shale under uniaxial compression with various dipping directions.

Excellent agreement exists between the stress distributions measured from the isotropic DEM model and those calculated from the analytical solutions. Under hydrostatically increased stress, particle size distribution plays an important role on the ultimate geometry of borehole breakout. Spiral-shaped shear fractures can be obtained in relatively homogenous model, while three V-shaped concentrated fractures arise in the more heterogeneous model. The critical hydrostatic pressure increases with the reduction of borehole diameter, accompanied with the dominant failure mechanisms transforming from tensile failure to shear failure of parallel bond. Under anisotropic far-field stress, the borehole breakouts in isotropic model turn out to be two V-shaped fractures aligning with the direction of minimum principal stress.

Existence of weakness significantly changes the stress concentration patterns around borehole wall as a result of deformation anisotropy. It is the combination of stress distribution and strength anisotropy that dominate the initiation of borehole breakout. Failure of smooth joint is found particularly prominent, while far-field stress anisotropy plays a secondary important role. Ultimate fractures concentrate in two regions which extend from the borehole in the direction normal to beddings under hydrostatic far-field stress, and slight rotation to the direction of minimum principal stress can be noted when the far-field stresses are unequal. The proposed numerical model can capture the development of stress-induced borehole breakout in anisotropic rock formation in laboratory scale and thus provides an avenue to the further study of borehole stability problems in field under more realistic conditions.

Acknowledgments
The research was funded by the National Natural Science Foundation of China (NSFC) (grant 51428902) and Open Research Fund of State Key Laboratory of Geomechanics and Geotechnical Engineering, Institute of Rock and Soil Mechanics, Chinese Academy of Sciences, grant Z014004. The authors would like to thank the two anonymous reviewers and the Associate Editor for their constructive comments and suggestions which greatly improved the quality of the manuscript. The data for this paper are available by contacting the corresponding author at fkwok8@hku.hk.

References

Addis, M., N. Barton, S. Bandis, and J. Henry (1990), Laboratory studies on the stability of vertical and deviated boreholes paper presented at SPE Annual Technical Conference and Exhibition, Soc. of Petrol. Eng.

Al-Ajmi, A. M., and R. W. Zimmerman (2006), Stability analysis of vertical boreholes using the Mogi–Coulomb failure criterion, *Int. J. Rock Mech. Min.*, *43*(8), 1200–1211.

Al-Busaidi, A., J. F. Hazzard, and R. P. Young (2005), Distinct element modeling of hydraulically fractured Lac du Bonnet granite, *J. Geophys. Res.*, *110*, B06302, doi:10.1029/2004JB003297.

Amadei, B. (1996), Importance of anisotropy when estimating and measuring in situ stresses in rock, *I. J. Rock Mech. Min. Sci. Geomech. Abstr.*, *33*(3), 293–325, doi:10.1016/0148-9062(95)00062-3.

Amadei, B., J. Rogers, and R. Goodman (1983), Elastic constants and tensile strength of anisotropic rocks paper presented at 5th ISRM Congress, Int. Soc. of Rock Mech.

Amann, F., E. Button, K. Evans, V. Gischig, and M. Blümel (2011), Experimental study of the brittle behavior of clay shale in rapid unconfined compression, *Rock Mech. Rock Eng.*, *44*(4), 415–430, doi:10.1007/s00603-011-0156-3.

Ambrose, J., R. W. Zimmerman, and R. Suarez-Rivera (2014), Failure of shales under triaxial compressive stress, in *The 48th US Rock Mechanics/Geomechanics Symposium*, Am. Rock Mech. Assoc., Minneapolis, MN.
Bahaaddini, M., G. Sharrock, and B. Hebblewhite (2013), Numerical investigation of the effect of joint geometrical parameters on the mechanical properties of a non-persistent jointed rock mass under uniaxial compression, *Comput. Geotech.*, *49*, 206–225.
Blümling, P., F. Bernier, P. Lebon, and C. Derek Martin (2007), The excavation damaged zone in clay formations time-dependent behaviour and influence on performance assessment, *Phys. Chem. Earth, Parts A/B/C*, *32*(8–14), 588–599, doi:10.1016/j.pce.2006.04.034.
Brudy, M., and M. D. Zoback (1999), Drilling-induced tensile wall-fractures: Implications for determination of in-situ stress orientation and magnitude, *Int.. J. Rock Mech. Min.*, *36*(2), 191–215, doi:10.1016/S0148-9062(98)00182-X.
Chiu, C.-C., T.-T. Wang, M.-C. Weng, and T.-H. Huang (2013), Modeling the anisotropic behavior of jointed rock mass using a modified smooth-joint model, *Int. J. Rock Mech. Min.*, *62*, 14–22, doi:10.1016/j.ijrmms.2013.03.011.
Cho, J. W., H. Kim, S. Jeon, and K.-B. Min (2012), Deformation and strength anisotropy of Asan gneiss, Boryeong shale, and Yeoncheon schist, *Int. J. Rock Mech. Min.*, *50*, 158–169.
Cho, N., C. D. Martin, and D. C. Sego (2007), A clumped particle model for rock, *Int. J. Rock Mech. Min.*, *44*(7), 997–1010.
Cook, B., M. Lee, A. DiGiovanni, D. Bronowski, E. Perkins, and J. Williams (2004), Discrete element modeling applied to laboratory simulation of near-wellbore mechanics, *Int. J. Geomech.*, *4*(1), 19–27.
Cundall, P. A. (2001), A discontinuous future for numerical modelling in geomechanics?, *P I Civil Eng-Geotec.*, *149*(1), 41–47.
Cundall, P. A., and O. D. Strack (1979), A discrete numerical model for granular assemblies, *Geotechnique*, *29*(1), 47–65.
Cundall, P., D. Potyondy, and C. Lee (1996), Micromechanics-based models for fracture and breakout around the mine-by tunnel, *Proceedings at International Conference on Deep Geological Disposal of Radioactive Waste, Winnipeg*, edited by J. B. Martino and C. D. Martin, Can. Nucl. Soc., Toronto.
Cuss, R. J., E. H. Rutter, and R. F. Holloway (2003), Experimental observations of the mechanics of borehole failure in porous sandstone, *Int. J. Rock Mech. Min.*, *40*(5), 747–761, doi:10.1016/S1365-1609(03)00068-6.
Diederichs, M. S. (2000), Instability of hard rockmasses: The role of tensile damage and relaxation, PhD Thesis, 566 pp., Univ. of Waterloo, Waterloo, Ont., Canada.
Ding, X., L. Zhang, H. Zhu, and Q. Zhang (2014), Effect of model scale and particle size distribution on PFC3D simulation results, *Rock Mech. Rock Eng.*, *47*(6), 2139–2156, doi:10.1007/s00603-013-0533-1.
Dresen, G., S. Stanchits, and E. Rybacki (2010), Borehole breakout evolution through acoustic emission location analysis, *Int. J. Rock Mech. Min.*, *47*(3), 426–435, doi:10.1016/j.ijrmms.2009.12.010.
Duan, K., and C. Kwok (2015a), Parametric study of smooth joint parameters on the behavior of inherently anisotropic rock under uniaxial compression condition, in *49th US Rock Mechanics/Geomechanics Symposium*, Am. Rock Mech. Assoc., San Francisco.
Duan, K., and C. Y. Kwok (2015b), Discrete element modeling of anisotropic rock under Brazilian test conditions, *Int. J. Rock Mech. Min.*, *78*, 46–56, doi:10.1016/j.ijrmms.2015.04.023.
Duan, K., C. Y. Kwok, and M. Pierce (2015a), Discrete element method modeling of inherently anisotropic rocks under uniaxial compression loading, *Int. J. Numer. Anal. Meth. Geomech.*, doi:10.1002/nag.2476.
Duan, K., C. Y. Kwok, and L. G. Tham (2015b), Micromechanical analysis of the failure process of brittle rock, *Int. J. Numer. Anal. Meth. Geomech.*, *39*(6), 618–634, doi:10.1002/nag.2329.
Ewy, R. T., and N. G. W. Cook (1990a), Deformation and fracture around cylindrical openings in rock—I. Observations and analysis of deformations, *Int. J. Rock Mech. Min. Sci. Geomech. Abstr.*, *27*(5), 387–407, doi:10.1016/0148-9062(90)92713-O.
Ewy, R. T., and N. G. W. Cook (1990b), Deformation and fracture around cylindrical openings in rock—II. Initiation, growth and interaction of fractures, *Int. J. Rock Mech. Min. Sci. Geomech. Abstr.*, *27*(5), 409–427, doi:10.1016/0148-9062(90)92714-P.
Fakhimi, A., F. Carvalho, T. Ishida, and J. F. Labuz (2002), Simulation of failure around a circular opening in rock, *Int. J. Rock Mech. Min.*, *39*(4), 507–515, doi:10.1016/S1365-1609(02)00041-2.
Fjær, E., and H. Ruistuen (2002), Impact of the intermediate principal stress on the strength of heterogeneous rock, *J. Geophys. Res.*, *107*(B2), 2032, doi: 10.1029/2001JB000277.
Fjær, E., and O.-M. Nes (2014), The impact of heterogeneity on the anisotropic strength of an outcrop shale, *Rock Mech. Rock Eng.*, *47*(5), 1603–1611, doi:10.1007/s00603-014-0598-5.
François, B., V. Labiouse, A. Dizier, F. Marinelli, R. Charlier, and F. Collin (2014), Hollow cylinder tests on boom clay: Modelling of strain localization in the anisotropic excavation damaged zone, *Rock Mech. Rock Eng.*, *47*(1), 71–86, doi:10.1007/s00603-012-0348-5.
Gaede, O., F. Karpfinger, J. Jocker, and R. Prioul (2012), Comparison between analytical and 3D finite element solutions for borehole stresses in anisotropic elastic rock, *Int. J. Rock Mech. Min.*, *51*, 53–63, doi:10.1016/j.ijrmms.2011.12.010.
Gaede, O., A. Karrech, and K. Regenauer-Lieb (2013), Anisotropic damage mechanics as a novel approach to improve pre-and post-failure borehole stability analysis, *Geophys. J. Int.*, *193*, 1095–1109.
Gatelier, N., F. Pellet, and B. Loret (2002), Mechanical damage of an anisotropic porous rock in cyclic triaxial tests, *Int. J. Rock Mech. Min.*, *39*(3), 335–354, doi:10.1016/S1365-1609(02)00029-1.
Haimson, B. (2007), Micromechanisms of borehole instability leading to breakouts in rocks, *Int. J. Rock Mech. Min.*, *44*(2), 157–173, doi:10.1016/j.ijrmms.2006.06.002.
Haimson, B. C., and I. Song (1993), Laboratory study of borehole breakouts in Cordova Cream: A case of shear failure mechanism, *Int. J. Rock Mech. Min. Sci. Geomech. Abstr.*, *30*(7), 1047–1056, doi:10.1016/0148-9062(93)90070-T.
Haimson, B., and H. Lee (2004), Borehole breakouts and compaction bands in two high-porosity sandstones, *Int. J. Rock Mech. Min.*, *41*(2), 287–301, doi:10.1016/j.ijrmms.2003.09.001.
Haimson, B., and J. Kovacich (2003), Borehole instability in high-porosity Berea sandstone and factors affecting dimensions and shape of fracture-like breakouts, *Eng. Geol.*, *69*(3–4), 219–231, doi:10.1016/S0013-7952(02)00283-1.
Itasca (2008), *PFC2D Particle Flow Code in 2 Dimensions*, Itasca Consulting Group Inc, Minneapolis, Minn.
Ivars, D. M., M. E. Pierce, C. Darcel, J. Reyes-Montes, D. O. Potyondy, R. P. Young, and P. A. Cundall (2011), The synthetic rock mass approach for jointed rock mass modelling, *Int. J. Rock Mech. Min.*, *48*(2), 219–244.
Katsman, R., and B. C. Haimson (2011), Modelling partially-emptied compaction bands induced by borehole drilling, *J. Struct. Geol.*, *33*(4), 690–697, doi:10.1016/j.jsg.2011.01.010.
Katsman, R., E. Aharonov, and B. C. Haimson (2009), Compaction bands induced by borehole drilling, *Acta Geotech.*, *4*(3), 151–162, doi:10.1007/s11440-009-0086-3.
Kirsch, G. (1898), Die theorie der elastizitaet und die bedeurfnisse der festigkeitslehre, *Z. Ver. Dtsch. Ing.*, *42*, 797–807.
Koyama, T., and L. Jing (2007), Effects of model scale and particle size on micro-mechanical properties and failure processes of rocks—A particle mechanics approach, *Eng. Anal. Boundary Elem.*, *31*(5), 458–472, doi:10.1016/j.enganabound.2006.11.009.

Kupferschmied, N., K. M. Wild, F. Amann, C. Nussbaum, D. Jaeggi, and N. Badertscher (2015), Time-dependent fracture formation around a borehole in a clay shale, *Int. J. Rock Mech. Min.*, *77*, 105–114, doi:10.1016/j.ijrmms.2015.03.027.

Kwok, C., and K. Duan (2015), DEM simulation of fracture process of inherently anisotropic rock under Brazilian test condition paper presented at 49th US Rock Mechanics/Geomechanics Symposium, 28 June–1 July 2015, San Francisco.

Labiouse, V., and T. Vietor (2014), Laboratory and in situ simulation tests of the excavation damaged zone around galleries in Opalinus Clay, *Rock Mech. Rock Eng.*, *47*(1), 57–70, doi:10.1007/s00603-013-0389-4.

Labiouse, V., C. Sauthier, and S. You (2014), Hollow cylinder simulation experiments of galleries in boom clay formation, *Rock Mech. Rock Eng.*, *47*(1), 43–55, doi:10.1007/s00603-012-0332-0.

Lan, H., C. D. Martin, and B. Hu (2010), Effect of heterogeneity of brittle rock on micromechanical extensile behavior during compression loading, *J. Geophys. Res.*, *115*, B01202, doi:10.1029/2009JB006496.

Lee, H., S. H. Ong, M. Azeemuddin, and H. Goodman (2012), A wellbore stability model for formations with anisotropic rock strengths, *J. Petrol. Sci. Eng.*, *96–97*, 109–119, doi:10.1016/j.petrol.2012.08.010.

Lee, H., T. Moon, and B. C. Haimson (2015), Borehole breakouts induced in arkosic sandstones and a discrete element analysis, *Rock Mech. Rock Eng.*, *49*, 1369–1388, doi:10.1007/s00603-015-0812-0.

Lee, M., and B. Haimson (1993), Laboratory study of borehole breakouts in Lac du bonnet granite: A case of extensile failure mechanism, *Int. J. Rock Mech. Min. Sci. Geomech. Abstr.*, *30*(7), 1039–1045, doi:10.1016/0148-9062(93)90069-P.

Mas Ivars, D. M., D. Potyondy, M. Pierce, and P. Cundall (2008), The smooth-joint contact model, *Proceedings of WCCM8-ECCOMAS*.

Meier, T., E. Rybacki, A. Reinicke, and G. Dresen (2013), Influence of borehole diameter on the formation of borehole breakouts in black shale, *Int. J. Rock Mech. Min.*, *62*, 74–85, doi:10.1016/j.ijrmms.2013.03.012.

Meier, T., E. Rybacki, T. Backers, and G. Dresen (2014), Influence of bedding angle on borehole stability: A laboratory investigation of transverse isotropic Oil shale, *Rock Mech. Rock Eng.*, *48*, 1535–1546, doi:10.1007/s00603-014-0654-1.

Niandou, H., J. Shao, J. Henry, and D. Fourmaintraux (1997), Laboratory investigation of the mechanical behaviour of Tournemire shale, *Int. J. Rock Mech. Min.*, *34*(1), 3–16.

Okland, D., and J. Cook (1998), Bedding-related borehole instability in high-angle wells Paper presented at SPE/ISRM rock mechanics in petroleum engineering, Soc. of Petrol. Eng.

Ong, S. H., and J. C. Roegiers (1993), Influence of anisotropies in borehole stability, *Int. J. Rock Mech. Min. Sci. Geomech. Abstr.*, *30*(7), 1069–1075, doi:10.1016/0148-9062(93)90073-M.

Papamichos, E., J. Tronvoll, A. Skjærstein, and T. E. Unander (2010), Hole stability of Red Wildmoor sandstone under anisotropic stresses and sand production criterion, *J. Petrol. Sci. Eng.*, *72*(1–2), 78–92, doi:10.1016/j.petrol.2010.03.006.

Potyondy, D. O., and P. A. Cundall (2004), A bonded-particle model for rock, *Int. J. Rock Mech. Min.*, *41*(8), 1329–1364.

Rahmati, H., A. Nouri, D. Chan, and H. Vaziri (2014), Simulation of drilling-induced compaction bands using discrete element method, *Int. J. Numer. Anal. Methods Geomech.*, *38*(1), 37–50.

Rawling, G. C., P. Baud, and T.-F. Wong (2002), Dilatancy, brittle strength, and anisotropy of foliated rocks: Experimental deformation and micromechanical modeling, *J. Geophys. Res.*, *107*(B10), 2234, doi:10.1029/2001JB000472.

Sokolnikoff, I. S., and R. D. Specht (1956), *Mathematical Theory of Elasticity*, McGraw-Hill, New York.

Van den Hoek, P. (2001), Prediction of different types of cavity failure using bifurcation theory paper presented at DC Rocks 2001, The 38th U. S. Symposium on Rock Mechanics (USRMS), Am. Rock Mech. Assoc.

Van den Hoek, P., D.-J. Smit, A. Kooijman, P. de Bree, C. Kenter, and M. Khodaverdian (1994), Size dependency of hollow cylinder stability paper presented at Rock Mechanics in Petroleum Engineering, Soc. of Petrol. Eng.

Vernik, L., and M. D. Zoback (1992), Estimation of maximum horizontal principal stress magnitude from stress-induced well bore breakouts in the Cajon Pass Scientific Research borehole, *J. Geophys. Res.*, *97*(B4), 5109–5119.

Zhang, J. (2013), Borehole stability analysis accounting for anisotropies in drilling to weak bedding planes, *Int. J. Rock Mech. Min.*, *60*, 160–170, doi:10.1016/j.ijrmms.2012.12.025.

Zhang, J., T. F. Wong, and D. M. Davis (1990), Micromechanics of pressure-induced grain crushing in porous rocks, *J. Geophys. Res.*, *95*(B1), 341–352.

Zheng, Z., J. Kemeny, and N. G. W. Cook (1989), Analysis of borehole breakouts, *J. Geophys. Res.*, *94*(B6), 7171–7182, doi:10.1029/JB094iB06p07171.

Zoback, M. D., D. Moos, L. Mastin, and R. N. Anderson (1985), Well bore breakouts and in situ stress, *J. Geophys. Res.*, *90*(B7), 5523–5530.

Zoback, M. D., C. A. Barton, M. Brudy, D. A. Castillo, T. Finkbeiner, B. R. Grollimund, D. B. Moos, P. Peska, C. D. Ward, and D. J. Wiprut (2003), Determination of stress orientation and magnitude in deep wells, *Int. J. Rock Mech. Min.*, *40*(7–8), 1049–1076, doi:10.1016/j.ijrmms.2003.07.001.